V. Motta, G. Quaranta
Linear Reduced-Order Model for Unsteady Aerodynamics of an L-Shaped Gurney Flap
Journal of Aircraft, Vol. 52, N. 6, 2015, p. 1887-1904
doi:10.2514/1.C033099

Physically-Based Linear Reduced Order Model for Unsteady Aerodynamics of a L-shaped Gurney Flap

Valentina Motta* and Giuseppe Quaranta†

via La Masa 34, Politecnico di Milano, Milano, 20156, Italy

The purpose of the work is to investigate the mechanism that underlies the development of unsteady loads by a novel L-shaped Gurney flap conceived to perform vibration control on rotorcraft blades. The device is combination of a spoiler with a Gurney flap. Exploiting the capabilities of a Reynolds-Averaged Navier-Stokes flow solver employing the overset mesh approach, several numerical simulations are carried out at low Mach number. These simulations are used to develop a physically-based linear reduced order model in the frequency domain for the unsteady lift and pitching moment of a NACA 0012 airfoil, considering as input the pitch and plunge harmonic oscillations of the airfoil, together with the oscillations of the L-shaped Gurney flap. The aerodynamic assessment of the L-tab shows that the behavior of the loads can be predicted using an equivalent flat-plate model to represent the airfoil composed by three segments: the first representing the fixed part of the airfoil, the second representing the longitudinal edge of the tab and the third representing the counter rotating vortical structures that appear behind the movable device. The same approach is used to model the static lift and moment enhancements, as due to an equivalent camber modification effect. The strong connection of the parameters of the reduced order model with the physical quantities is highlighted, as well as its predictive capability for arbitrary parameters of the imposed motion laws.

Nomenclature

a_n n-th coefficient within the analytical computation of loads

*Postdoctoral fellow, Dipartimento di Scienze e Tecnologie Aerospaziali
†Assistant Professor, Dipartimento di Scienze e Tecnologie Aerospaziali

b unitary semi-chord within the analytical model

$c_k = 2b$ airfoil chord within the analytical model [m]

c_{ref} reference sound speed [m/s]

C_d drag coefficient

C_ℓ lift coefficient

C_m pitching moment coefficient

C_P pressure coefficient

f functional to be minimized within the model order reduction

F generic aerodynamic force [N]

g space dependent upwash velocity within the analytical model

h airfoil position for the plunge motion [m]

$\mathfrak{I}$ imaginary part of a generic complex parameter

k reduced frequency, $\omega b/U$

M freestream Mach number

$\mathbf{p}$ array of free parameters within the model order reduction

P_n upwash n-th coefficient within the analytical model

$\mathfrak{R}$ real part of a generic complex parameter

Re freestream Reynolds number

t time [s]

U freestream velocity [m/s]

v vertical component of the perturbation velocity [m/s]

$|V|$ local velocity magnitude [m/s]

x position along the chord within the analytical model [m]

z position coordinate perpendicular to the chord [m]

$\tilde{(\cdot)}$ variables in the Fourier transform domain

α angle of attack [deg.]

β L-tab deflection angle, positive upward [deg.]

φ phase of a generic complex quantity.

ΔC_P difference of C_P between the lower and the upper side of the body

θ x-transformation coordinate, $x = \cos\theta$

χ_w CRV-related chord extension

ω angular velocity [1/s]

Subscript

0 the pole of the pitching moment

k quantity related to the analytical model

n index for the series terms within the analytical model

N number of terms of the truncated series within the analytical model

f quantity related to the equivalent L-tab within the analytical model

c/w quantity related to the equivalent trim tab within the analytical model

I. Introduction

The Gurney Flap (GF) was originally designed for the racing car of Dan Gurney to increase the vehicle downforce generated by the rear inverted wing [1]. Ever since, the GFs have also attracted attention of aircraft and rotorcraft designers as a very effective high-lift device. Moreover, GFs are successfully applied in wind turbines and in turbomachinery.

The GF effectiveness is due its simplicity: a flat plate attached to the trailing edge (TE) and perpendicular to the chord line. On the contrary, classical high lift devices are very complicated, both in terms of aerodynamics that control their functioning, and mechanical systems necessary to activate them, requiring a high level of maintenance operations. Liebeck [2] was among the first to study the behavior of Gurney flaps for aeronautical applications. His studies showed that two counter rotating vortices are generated behind the Gurney flap because the flow is forced to turn around the perpendicular plate at the TE. The intersection point of the streamlines coming from the pressure and from the suction side is shifted away from the TE. As a consequence, the location of the Kutta condition is shifted downstream the TE so that, in terms of load, it is equivalent to what can be obtained by a longer effective chord and a more cambered airfoil. The interpretation

proposed by Liebeck in Ref. [2] on the aerodynamic effects of GFs was confirmed later. Experiments conducted on airfoils equipped with GFs highlighted the capability of these devices to significantly increase lift without severe drawbacks in terms of drag increment [3–10]. Several numerical computations have investigated the behavior of GFs [9, 11–15]. These studies highlighted how such movable devices allow to increase the lift, and in particular the maximum lift and the lift to drag ratio. Kentfield [3] developed a semi-empirical formulation to compute the lift and drag augmentations on airfoils equipped with a GF as a function of the height of such devices.

Recently, large interest focused on movable aerodynamic surfaces for aerodynamic performance improvement, alleviation of vibratory loads, flutter suppression and modification of the vortical wake. Several authors worked on the application of movable trailing edge flaps on rotorcraft blades for vibratory load control, see Refs. [16–20], and for the mitigation of negative effect associated with dynamic stall, see Refs. [21–23]. Because a GF has considerably less inertia than a traditional flap, smaller forces are expected to be required to actuate the system. Consequently, a larger bandwidth can be achieved together with a reduced modification of the structural stiffness of the blades.

Gerontakos and Lee [24] performed experimental measurements on a NACA 0012 section equipped with fixed GF-like strips both on the pressure and on the suction side of the airfoil. They showed that trailing edge strips can improve the performance of oscillating airfoils, in dynamic stall conditions. Tang and Dowell [25] validated a numerical model of a fixed GF on an oscillating airfoil against the experiments of Ref. [24]. They showed using numerical computations that an oscillating Gurney flap brings additional benefits for deep-stall cases. Then, in Ref. [26], experiments were carried out on an oscillating NACA 0012 equipped with an oscillating GF, reaching the same conclusions of the numerical work, that an oscillating small strip located near the trailing edge can be used for active aerodynamic flow control of a lifting surface.

Kinzel et al. [27] performed several steady and unsteady numerical simulations for various flow conditions over a S903 section equipped with GFs, referred to as Miniature Trailing edge Effectors (MiTEs). Such simulations gave an overview on the possible usage of MiTEs both to improve performance and to reduce vibratory loads on helicopter blades. Additionally, they investigated the

effect of chordwise positioning of the GF, showing that increased upstream positioning enlarges the hysteresis loop, degrades the lift enhancement, increases drag and decreases the nose-down pitching moment. Similar limits were found also in Refs. [10, 14, 28, 29]. Matalanis et al. [30] carried out 2D and 3D simulations, together with experimental measurements, on a VR-12 section equipped with a deployable GF. They investigated the effects of the actuation frequency of the movable device on the vibratory moment coefficient, showing by CFD-CSD coupled analysis on a model of the UH-60A that significant reduction of vibratory loads can be achieved. Min et al. [31] by using CFD-CSD simulations, showed significant reduction on the classical HART-II test case with deployable GF. Liu et al. [32] investigated by numerical simulations the effect of several Gurney flap-like devices on a NACA 0012 airfoil. They used numerical CFD computations as a reference to develop a Reduced Order Model (ROM) for the unsteady loads developed by the airfoil section equipped with his movable device. This model was used within a comprehensive solver and an active control system was designed to effectively reduce vibratory loads on a helicopter rotor.

Despite the progress in understanding the behavior of these movable devices, the integration of an active GF on a helicopter blade is still a very challenging design problem. In particular it is necessary to stow the deployable device, together with the actuation mechanism, at the TE, complying with weight and balance constraints related to the aeroelastic behavior of the blades. Moreover classical sliding actuation solutions, widely used for fixed wing GFs, are likely to fail, under high centrifugal loads that affect rotor blades. Palacios et al. [33] carried out several experimental tests to investigate the behavior of MiTEs under centrifugal loads comparable to those encountered on rotor blades. They found that such devices can operate in these conditions. Moreover, the power requirements of GF like devices were significantly lower than those of classical plain flaps. They proposed a new pneumatic actuation system for movable GFs, which exploits the pressure radial gradients within the rotor blades.

To avoid both stowage and actuation issues, Zanotti et al. [34, 35] proposed an L-shaped tab that is a combination between a TE spoiler, i.e. a classical split flap, and a GF, applied at the TE of a helicopter blade section. The positive effects of a combination between a TE flap, and a GF

are emphasized also by Lee [36]. This concept has the additional advantage of locating the GF on the trailing edge [34, 35],therefore maximizing its performance [8]. Experimental measurements carried out by Zanotti et al. showed that this novel L-shaped tab could be exploited both downward deployed, as a GF, and upward deflected, as a classical TE flap, to mitigate the negative effects of dynamic stall.

To verify the capabilities of this new device also to control vibratory loads in flow conditions different from those typical of dynamic stall, the behavior of the unsteady aerodynamic forces from oscillations of the airfoil and of the L-tab is investigated numerically by means of CFD. A preliminary numerical assessment of the capabilities of this device was reported in Ref. [15]. The analyses highlighted how the L-tab allowed for the enhancement of performance both for small and high angles of attack in steady state conditions. Additionally, simulations carried out for small amplitude pitch oscillations of the section equipped with such L-tab showed the potential suitability of such device, both downward and upward deflected, for vibration reduction on helicopter blades.

For the design process and the development of control strategies, it is useful to develop a Reduced Order Model (ROM) starting from CFD simulations.

Liu and Montefort [37] proposed an analytical interpretation of steady effects of GFs on the basis of the thin airfoil theory. An extension of the thin-plate approach to the unsteady domain was proposed by Kinzel et al. [38]. The model was based on the formulation of Hariharan and Leishman [39], which was originally developed for airfoils equipped with a classical flap, and essentially it looks for an equivalent flap size that returns an indicial response that best approximates the indicial response of the GF obtained from a CFD computation. The formulation allows considering of the effects of Mach number. These linear models are able to capture the harmonic components of the aerodynamic loads. An extension has been proposed in Ref. [40] to model also the non-harmonic disturbances visible in the results of the CFD simulations.

A different approach is followed here, with the aim of developing a physically based linear ROM for the harmonic components of the unsteady lift and moment that does not require to run a CFD indicial response simulation, but relies on physical flow features, such as the size of the Counter Rotating Vortices (CRV) area developed past the L-tab. The accurate reproduction of the

first harmonic, i.e. the same harmonic of the input, is the primary interest of the ROM in view of the application of Higher Harmonic Controls (HHC) for vibration reduction.

The present work is focused on the development of a ROM for a NACA 0012 section equipped with a TE L-tab, with the shape of the movable device adopted by Ref. [35]. The primary effect of the L-tab consists of a modification in the effective blade section mean line. Consequently, similar to the approach followed by other authors, a flat-plate approximation approach can here be effectively employed. In this case the analytical formulation of Küssner and Schwarz [41] (KS) is selected to build the approximating model, because it is able to deal with arbitrarily shaped mean lines. As a result the ROM modeled, is found to reproduce correctly the equivalent mean line of the blade section equipped with the L-tab. In particular, the inclination and the length of the Counter Rotating Vortices (CRV) past the L-tab, is accurately represented by the final segment of the ROM mean line. At this stage no attempt has been made to investigate the effect of Mach number, so low Mach number CFD simulations have been employed to identify the parameters of the ROM model. However, extension to higher Mach numbers could be straightforward using the identified equivalent flat-plate model in conjunction with the Hariharan and Leishman [39] formulation.

II. Geometrical and Computational Fluid Dynamics Models

Figure 1 shows the L-tab geometry positioned on the TE of the airfoil. The device resembles the one employed by Zanotti et al. [35] in their dynamic stall experiments. However, a symmetric NACA0012 airfoil section is adopted here instead of the NACA23012 used in the experiments. The rationale for the employment of a symmetrical section is twofold: 1. This choice allows a direct comparison with several experimental and numerical computation available in literature, and 2. Allows to highlight clearly the equivalent camber modifications induced by the presence of the Gurney tab at the TE.

The L-tab length chordwise is 20%c while the height of the tab is 1.33%c. The L-tab protrudes 1.01%c from the airfoil pressure side, being the geometry of the clean airfoil cut before the trailing edge. This is consistent with the GF heights found in literature, that commonly range between

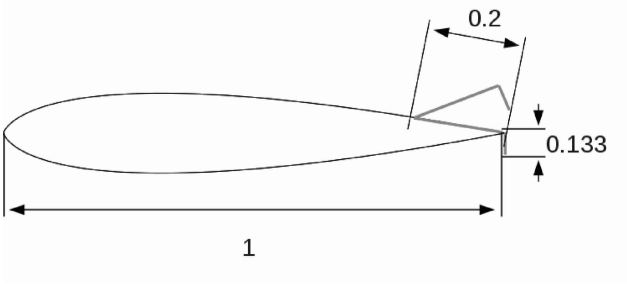

Figure 1. Schematic of the NACA 0012 section equipped with the TE L-tab.

0.5%c to 3%c [8].

The device is designed to be in the rest position when it is rotated upward by 4 deg., measured starting from the position where the spoiler is supported by the suction surface. In this condition, the end of the vertical prong lies aligned with the pressure side corner of the trailing edge. Therefore, the baseline configuration of the resulting airfoil presents a divergent TE. Several experimental tests [42, 43] have shown that such a divergent TE configuration could be effective in particular for transonic flow conditions, being these latter not unusual for rotorcraft blade sections.

The ROSITA (ROtorcraft Software ITAly) solver [44] was used to perform numerical CFD simulations of the L-tab to assess its performances. This solver integrates numerically the RANS equations, coupled with the one-equation turbulence model of Spalart-Allmaras [45] even in moving, overset, multi-block grids. A fully turbulent flow was assumed for the numerical computations. The equations are discretized in space by means of a cell-centered finite-volume implementation either of the Roe's scheme, which is used in this work, or of the Jameson's one, with scalar and matricial numerical viscosity. Second-order accuracy is obtained through the use of Monotonic Upstream-Centered Scheme for Conservation Laws (MUSCL) [46,47] extrapolation supplemented with a modified version of the Van Albada limiter introduced by Venkatakrishnan [48]. The viscous terms are computed by the application of the Gauss theorem and using a cell-centered discretization scheme. Time advancement is carried out with a dual-time formulation, employing a second order backward differentiation formula to approximate the time derivative and a fully unfactored implicit scheme in pseudo-time. The generalized conjugate gradient (GCG), in conjunction with a block incomplete lower-upper preconditioner, is used to solve the resulting linear system, see Refs. [44, 49, 50].

To deal with parts in relative motion with respect to each other, a system of two overlapped structured grids was used. The former background C-type grid of 79,320 elements extends from the airfoil up to 25 chords-distant far-field boundary. In particular, 412 elements are placed on the airfoil, 30 elements through the boundary layer, 159 along the wake and 40 in the radial direction from the end of the boundary layer up to the far-field. The latter overlapping grid, composed of 45,281 elements, is realized around the L-tab and it has rectangular shape. This has width of three times the length of the tab, i.e., $4\%c$, and height equal to twice the length of the movable device, i.e., $40\%c$. The overlapped grid is composed of 230 elements located on the L-tab, 25 elements located through the L-tab boundary layer, 25 elements in the longitudinal and transverse directions, from the end of the boundary layer up to the grid boundaries. The two grids are coupled by the

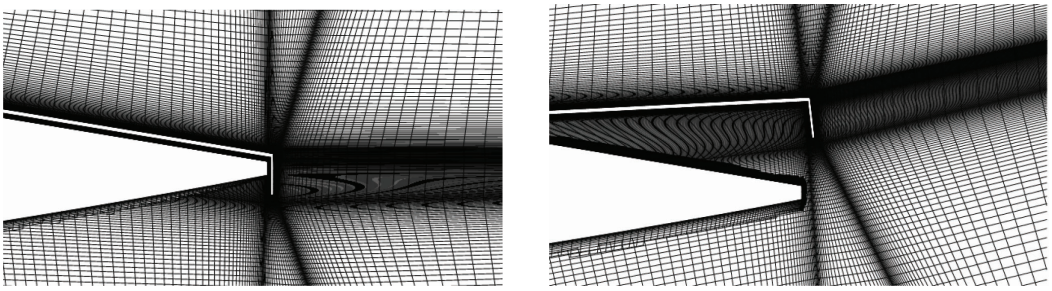

a) L-tab deflected downward. **b) L-tab deflected upward.**

Figure 2. System of overset grids used for the numerical computations.

numerical solver through the Chimera algorithm [44], and a narrow connection channel between the pressure and suction side is created. Figure 2 represents the reference computational grid, resulting after the Chimera interpolation.

Numerical computations were carried out to investigate the sensitivity of the force coefficients to the slot between the airfoil and the tab. A second computational grid was realized around a monolithic solid geometry, composed by the union of the clean airfoil plus the L-tab downward deflected. Steady state computations, showed that for small angles of attack, which are the concern of this work, relative differences of less that 1% were obtained in terms of lift and moment coefficient between the cases with or without the slot. Larger differences were obtained instead at high angles of attack where the presence of the slot delays significantly the stall. The influence of the slot on the airloads is discussed later.

All simulations were carried out at a Reynolds number of 10^6 and a Mach number of 0.117, comparable to those of the experiments of Ref. [35].

Steady state CFD simulations, see Fig. 3, show that behind the present tab two CRV close to the TE appear, both in the upward and downward deflected L-tab configurations, as expected for a Gurney flap-like device. Figure 4 shows the C_P distribution on the clean airfoil compared to those obtained with the L-tab deflected upward and downward. The comparisons of the enclosed areas at the different L-tab rotations demonstrate that the downward deflection causes an increase of the sectional lift coefficient, while the upward deflection causes a reduction of lift. Figure 4 also shows how at the TE the pressure coefficient of the pressure and suction sides are unequal.

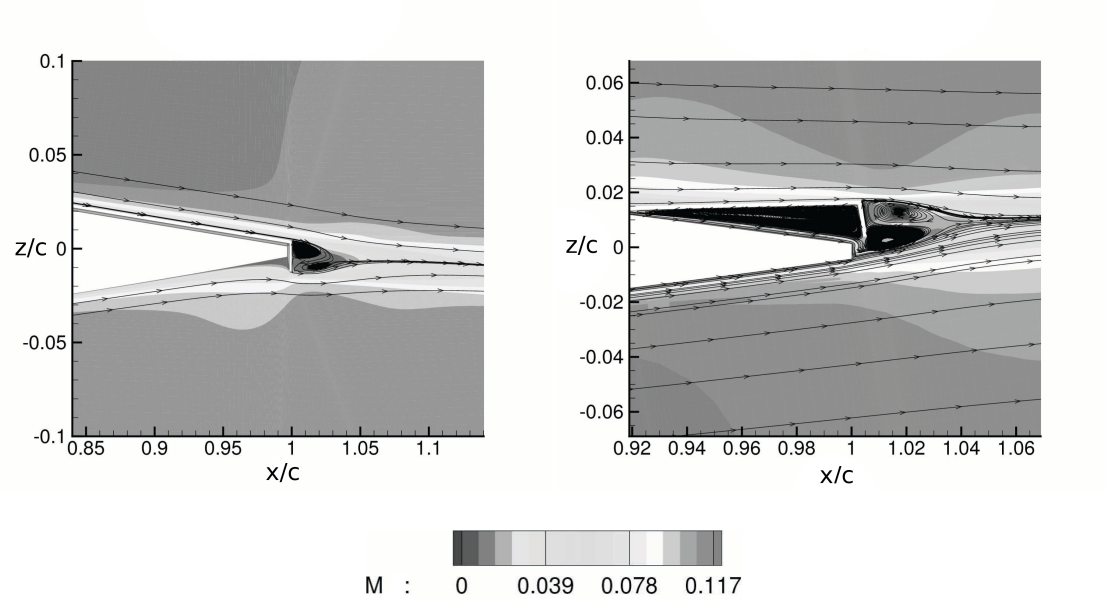

Figure 3. Mach number field and streamlines close to the L-tab in downward, $\beta_{\text{L-tab}} = 0$ deg., and upward, $\beta_{\text{L-tab}} = 9$ deg., positions. Angle of attack $\alpha = 0$ degrees.

For the present numerical work the chordwise length of the L-tab is doubled with respect to the 10%c-long movable device of the experiments by Zanotti et al. [35]. The numerical analyses revealed that a longer L-tab performs better in delaying the static stall when deflected upward. The flow fields of the velocity magnitude normalized with respect to the reference speed of sound, $c_{\text{ref}} = 346$ m/s, obtained at $\alpha = 18$ deg. and $\beta_{\text{L-tab}} = 27$ deg. for the 10%c and the 20%c L-tabs are shown in Fig. 5. With the shorter tab, the flow is fully separated on the suction side, whereas with the longer L-tab configuration a region of reattachment can be observed, reducing

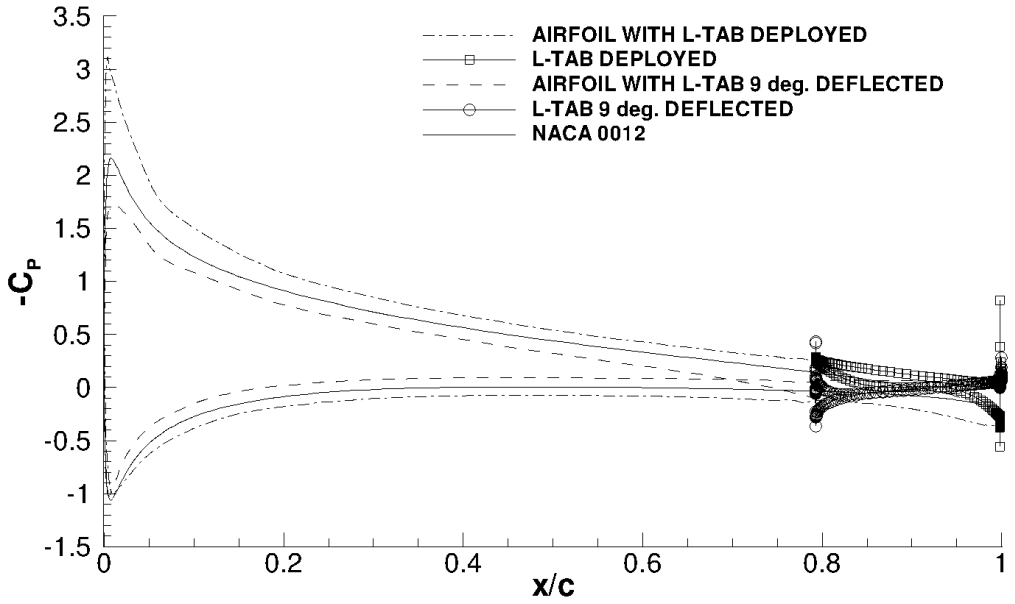

Figure 4. Comparison of the pressure coefficient distribution on the NACA 0012 with and without L-tab. Angle of attack α = 6 deg.

the lift coefficient losses typical of the post-stall conditions. The force coefficients computed for $\beta_{\text{L-tab}}$ = 27 deg. at moderate and high angles of attack are shown in Fig. 6. where it can be seen that the longer tab performs better.

A. Validation of the Numerical Results

To ensure the reliability of the computations, a convergence analysis was performed. The convergence in the pseudo-time is investigated by varying the number of iterations for the implicit integration. Table 1a shows that the pseudo time convergence was achieved with 5,000 iterations for the steady computations. The difference between lift, drag and moment coefficients computed with respect to the reference case, where 10,000 pseudo-time iterations were used, was always smaller than 1.2%.

The spatial convergence was analyzed by halving and doubling the grid elements of the 124,601 cells reference mesh. Table 1b shows the sensitivity of the aerodynamic loads to the spatial resolution of the grid. By doubling the refinement of the reference grid, the maximum

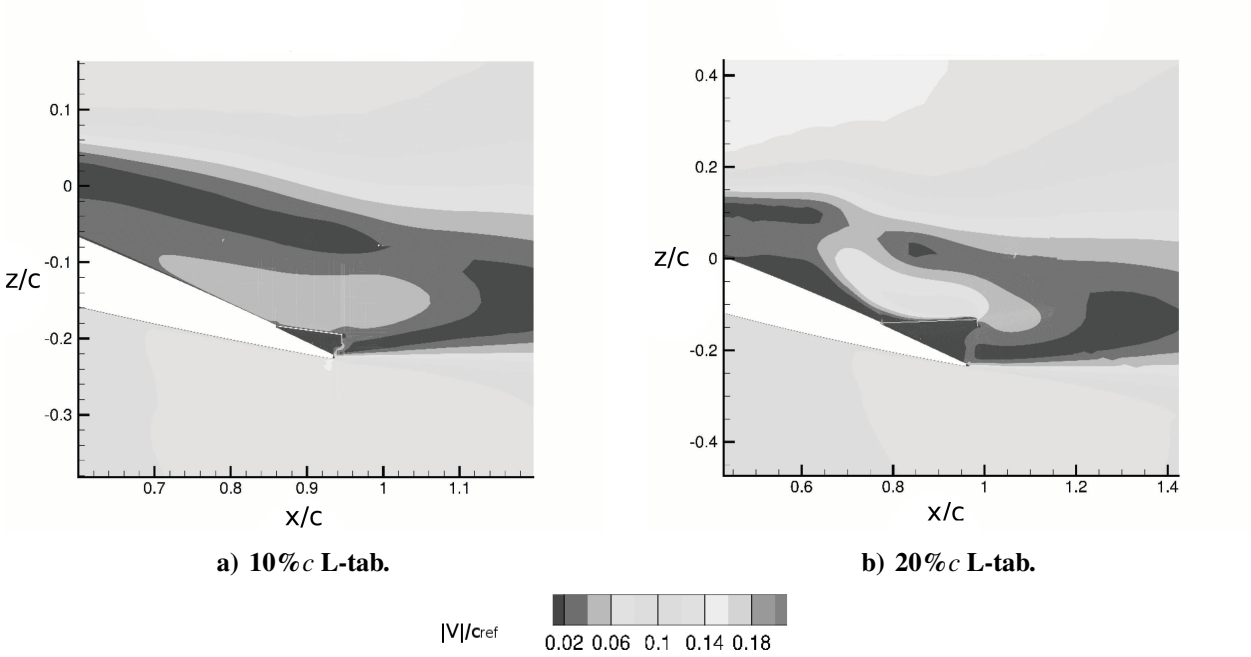

a) 10%c L-tab. **b) 20%c L-tab.**

Figure 5. Local velocity magnitude normalized to the reference sound speed $c_{\mathbf{ref}}$ = 346 m/s, for the 10%c (left) and the 20%c (right) long L-tab, α = 18 deg. and $\beta_{\mathbf{L\text{-}tab}}$ = 27 deg.

difference in the aerodynamic loads is for the drag coefficient, where is equal to 8% referred to the reference test case computed on a grid of 124,601 elements and with 5,000 pseudo time steps; significantly smaller differences were found for the lift and moment coefficients.

The geometrical configuration with the L-tab downward deflected was used for the convergence analyses. Indeed this configuration appeared to be the most challenging for numerical computations, primarily because of the recirculating flow area, which is generated upstream the tab when it protrudes from the airfoil lower side. As a consequence high gradients are expected in the flow quantities beside the tab. Moreover, the very small slot between the airfoil and the tab is potentially additional cause of numerical issues.

Because the L-tab is expected to generate unsteady phenomena on the flow field, the convergence to an average steady state for time-independent configurations, was verified by means of unsteady computations. Figure 7 shows how a steady state solution is reached for each of the force coefficients at low incidence. Hence, in this regime with small angles of attack any unsteady phenomena do not seem to severely affect aerodynamic loads, and it is consistent with the largely used experimental data by Abbot [51]. Consequently the steady flow approximation is appropriate with

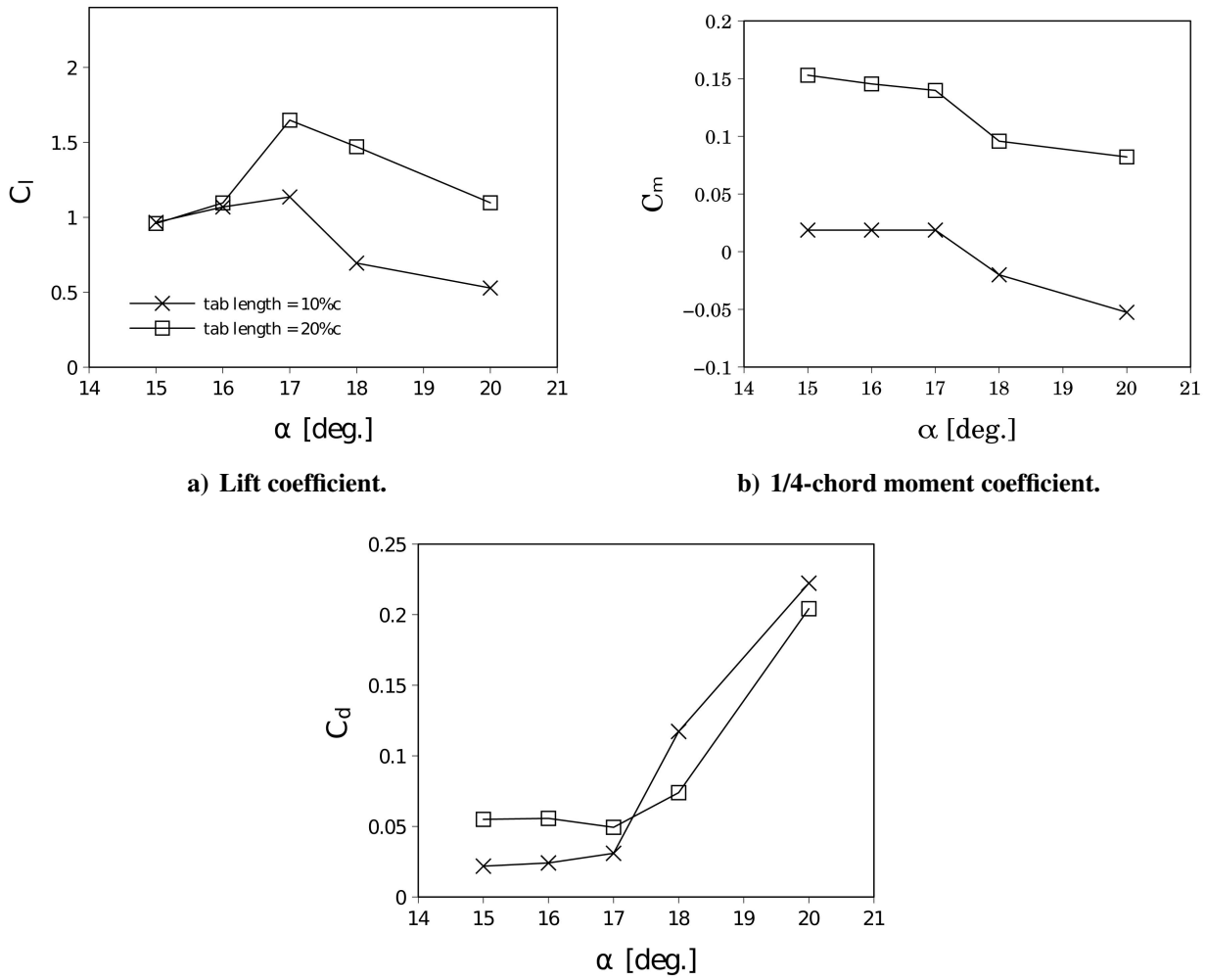

a) Lift coefficient.

b) 1/4-chord moment coefficient.

c) Drag coefficient.

Figure 6. Force coefficients for the 10%c and the 20%c long L-tabs at moderate and high angles of attack for $\beta_{\text{L-tab}}$ = 27 deg.

the L-tab in fixed position.

Comparisons of the current numerical computations with experimental data from Ref. [28] are reported for the clean airfoil and for the configuration with the L-tab deployed downward. There are no experimental data for the upward deflected configuration. Figures 8a and 8b show the comparison between the computed pressure coefficient and the experimental measurements of Li et al. [28] at angle of attack α = 4 deg. for a classical GF 1.5%c long. Good agreement is found between the numerical and the experimental results, both for the clean NACA 0012 airfoil and for the section equipped with the downward deployed L-tab. In particular, the peaks in the leading edge area, crucial in affecting the resulting lift, are well captured by the computations. Figure 8b

Table 1. Pseudo-time steps and spatial resolution convergence analysis performed on aerodynamic loads at $\alpha = 0$ deg. and with the tab downward deployed. The number of pseudo-time steps is fixed at 5,000; $M = 0.117$, $Re = 10^6$.

a) Pseudo-time steps convergence analysis.

P-T steps	C_l	C_m	C_d
5,000	0.1468	-0.0686	0.0090
10,000	0.1451	-0.0679	0.0089
40,000	0.1450	-0.0679	0.0089

b) Grid convergence analysis.

Elements	C_l	C_m	C_d
63,281	0.3001	-0.1262	0.0087
124,601	0.1468	-0.0686	0.0090
202,569	0.1383	-0.0636	0.0082

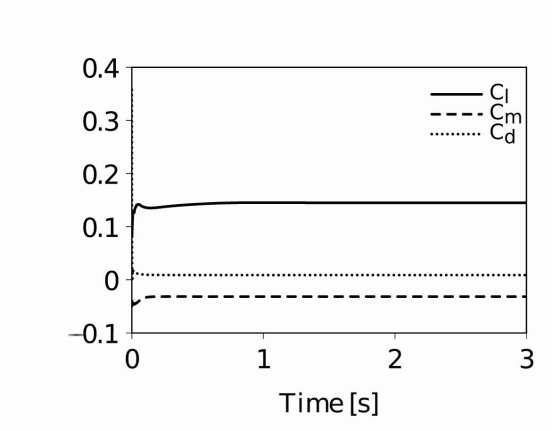

Figure 7. Time history of the force coefficients during an unsteady RANS simulation with L-tab downward deflected in fixed position, $\alpha = 0$ deg.

also shows that the finite difference of pressure between the lower and the upper side, developed at the trailing edge by the GF and by the L-tab, is reasonably similar.

Figure 9 shows the comparison of lift, 1/4-chord moment and drag coefficients between the computations and the experiments of Li et al. [28] on the clean NACA 0012 section. Good agreement was found for all force coefficients. Figure 10 shows the same comparison with the experiments of Li et al. [28] on the NACA 0012 section equipped with the 1.5%c GF, and also here an agreement was found in the range of angle of attack where the flow separation is not involved. The disagreement in terms of the stall onset prediction, for both the clean airfoil as well as the section with the trailing edge device, found by other authors too [32], may be because of the assumption of fully turbulent flow and to limitations of the turbulence models of the present computations.

Many CFD results on GFs are available in the literature, [25, 30, 33], which employ computational grids with no slots between the GF surface and the airfoil. Because the grid of the present

work is conceived to present a finite slot between the airfoil and the L-tab it is important to estimate the effects of such a gap on the numerical solutions. Figure 11 shows the aerodynamic loads computed at angles of attack ranging between $\alpha = -3$ deg. and $\alpha = 20$ degrees. For low angles of attack, a behavior similar to the slotted configuration was observed. A remarkably different behavior was observed at medium to high angles of attack. The non-slotted configuration significantly foregoes the prediction of the angle of attack of the stall onset, which is found well below 15 deg.; see Fig. 11. This result is consistent with other CFD computations, e.g. Refs. [32, 33].

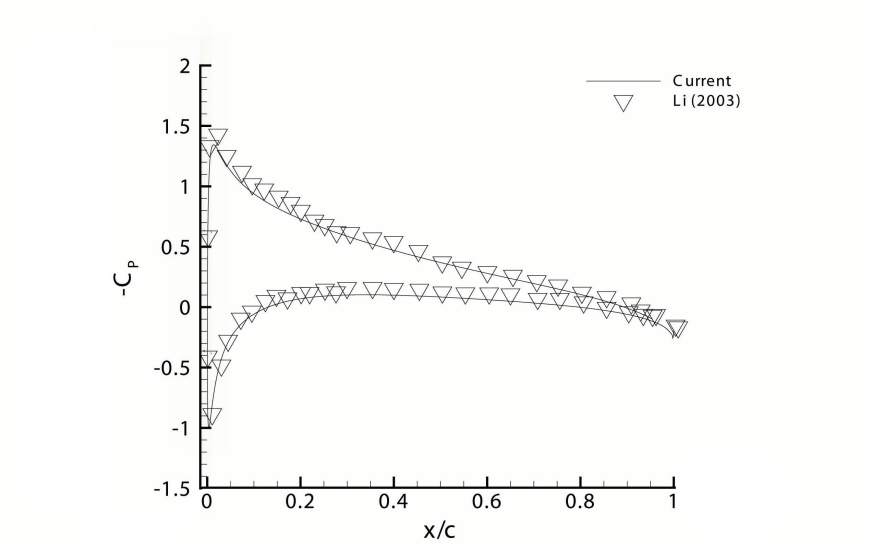

a) NACA 0012 clean airfoil.

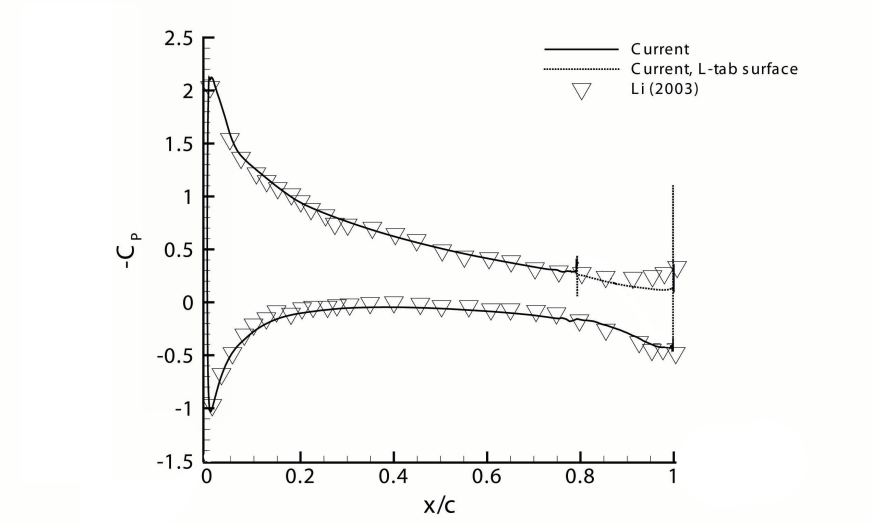

b) NACA 0012 with L-tab/GF downward deflected.

Figure 8. Comparison of the steady state pressure distribution computed at $\alpha = 4$ deg. with experimental data on a clean NACA 0012.

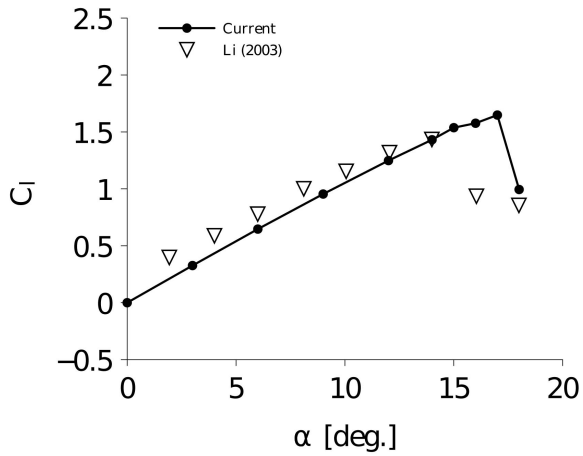

a) Lift coefficient.

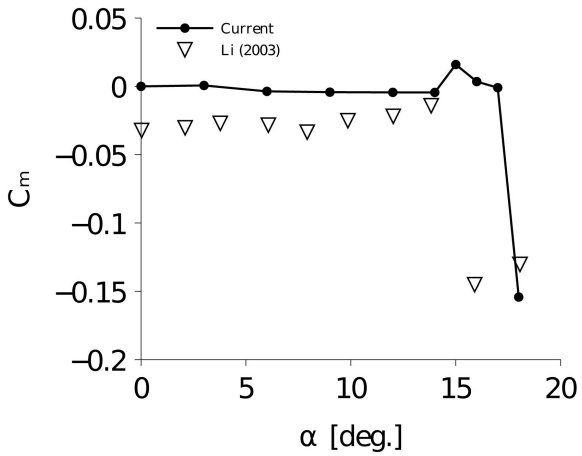

b) 1/4-chord moment coefficient.

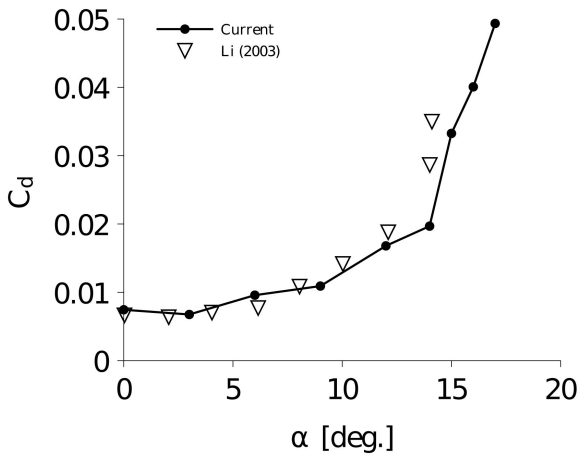

c) Drag coefficient.

Figure 9. Comparison of the steady state force coefficients with experimental data on the clean NACA 0012 section.

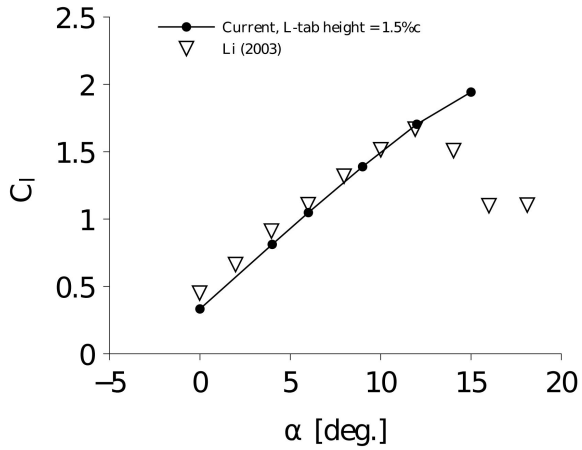

a) Lift coefficient

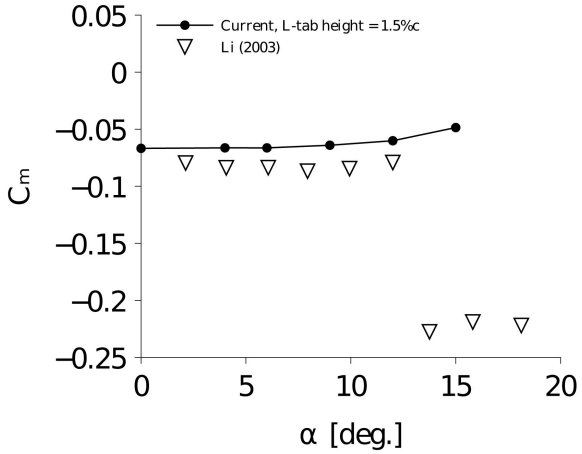

b) 1/4-chord moment coefficient

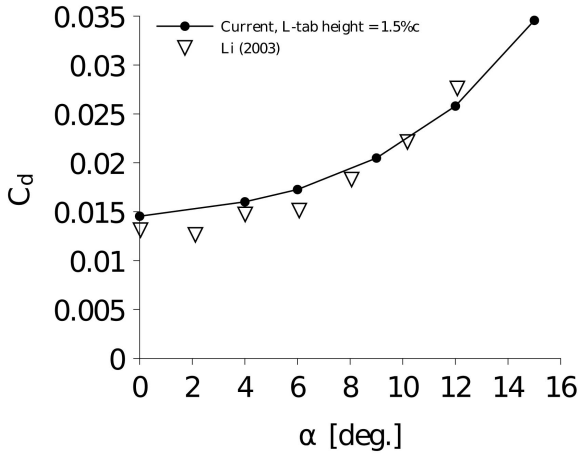

c) Drag coefficient

Figure 10. Comparison of the steady state force coefficients with experimental data on the NACA 0012 section equipped with 1.5%c GF.

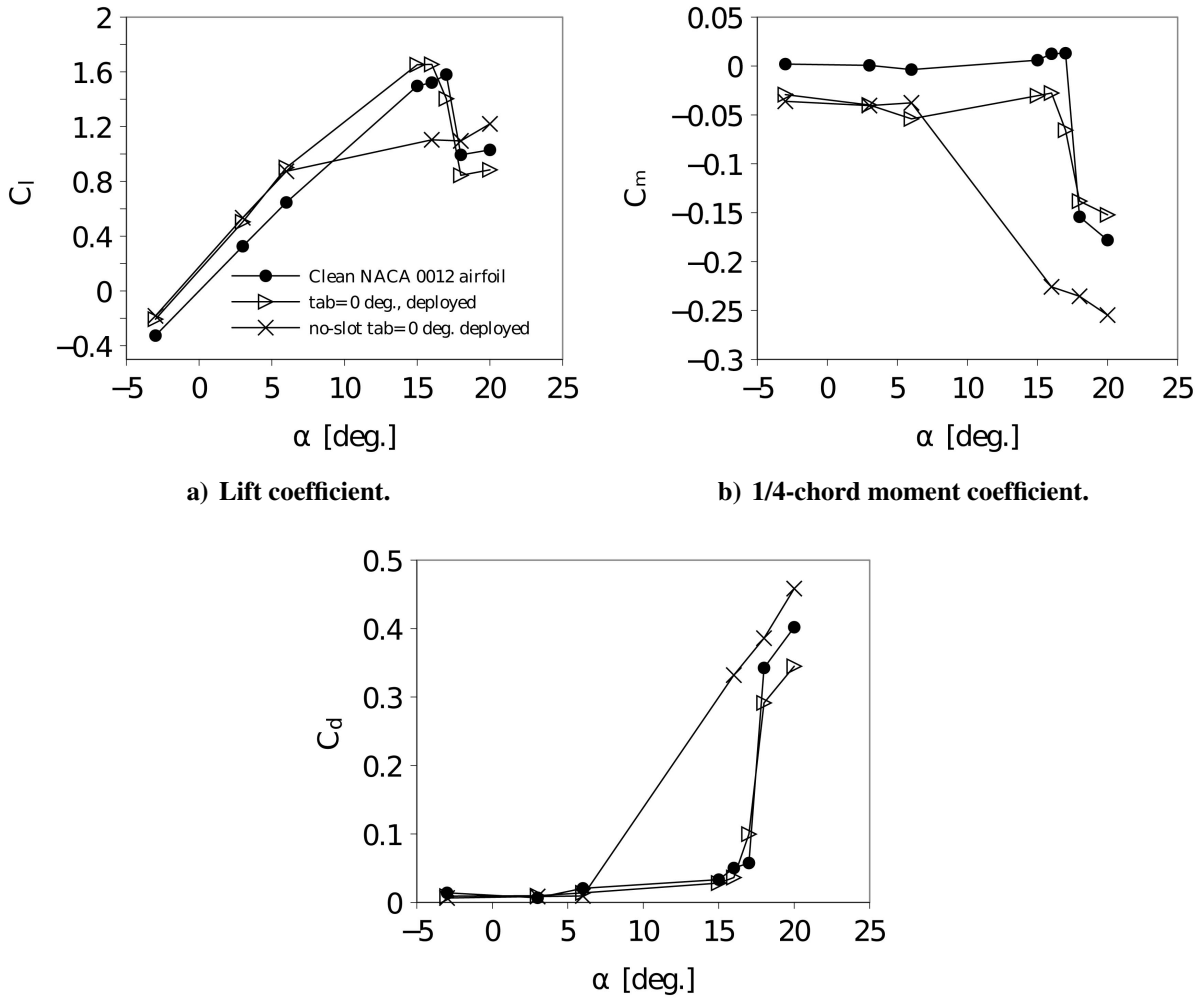

a) Lift coefficient.

b) 1/4-chord moment coefficient.

c) Drag coefficient.

Figure 11. Force coefficients for the slotted and the not-slotted L-tab, together with the baseline airfoil.

III. Reduced Order Model for an Airfoil Equipped with the L-tab

The analytical reduced order model developed in this work has its cornerstone in theory of Küssner-Schwarz (KS) [41, 52]. This theory is based on the hypothesis of incompressible potential fluid flow, and so it is linear and uses thin-airfoil approach. In accordance with the small perturbation hypothesis, the aerodynamic solution of the unsteady flow around airfoils can be obtained (see [41, 53]) as a linear combination of elementary solutions corresponding to the separate contributions of angle of attack, camber and thickness distribution. The KS formulation allows for a a quick and accurate computation of the pressure distribution in terms of differences between the lower and the upper side, for an arbitrarily shaped mean line affected by any kind of motion, as far as the assumption of small perturbations is valid. The capability of the KS model to deal with any kind of motion, comes directly from theoretical foundation of the model. Because it is based on the Fourier decomposition of the velocity distribution along the mean line, then an airfoil moves according to a generic harmonic law:

$$z(x,t) = |\tilde{z}(\omega,x)|\mathrm{e}^{(\mathrm{j}\omega t+\varphi_z(\omega,x))}, \tag{1}$$

where $\tilde{(\cdot)}$ is the symbol used for the Fourier transformed variables and φ_z represents the phase of $\tilde{z}$. The upwash velocity from the airfoil motion can be computed using:

$$v(x,t) = \frac{Dz}{Dt} = \frac{\partial z}{\partial t} + \frac{\partial z}{\partial x}\frac{\partial x}{\partial t} = \frac{\partial z}{\partial t} + U\frac{\partial z}{\partial x}. \tag{2}$$

The Fourier series of the spatial velocity distribution allows for the computation of the upwash coefficients P_0, ...P_n, i.e.,

$$v(\theta,t) = g(\theta)\mathrm{e}^{(\mathrm{j}\omega t+\varphi(\theta))} = -U\mathrm{e}^{\mathrm{j}\omega t}\left(P_0 + 2\sum_{n=1}^{\infty} P_n \cos n\theta\right), \tag{3}$$

where θ is an angular abscissa that corresponds to the position x along the airfoil chord, through the classical transformation $x = b\cos\theta$, with $2b$ the chord of the airfoil. The upwash coefficients

are:

$$P_n = -\frac{1}{U\pi}\int_0^{\pi} g(\theta)\mathrm{e}^{\mathrm{j}\varphi(\theta)}\cos n\theta \mathrm{d}\theta \tag{4}$$

Küssner and Schwarz [41, 52] proved that the difference of pressure coefficient can be expressed as a Fourier series:

$$\Delta C_p(\theta, t) = \mathrm{e}^{\mathrm{j}\omega t}\left(4A_o \tan\frac{\theta}{2} + 8\sum_{n=1}^{\infty} A_n \sin n\theta\right), \tag{5}$$

with the A_n coefficients that can be expressed as function of the upwash coefficients, i.e.,

$$A_0 = C(k)\left(P_0 + P_1\right) - P_1 \tag{6}$$

$$A_n = P_n + \frac{\mathrm{j}k}{2n}\left(P_{n-1} - P_{n+1}\right) \qquad \forall n > 0 \tag{7}$$

In Eqs. 7 k is the reduced frequency $k = \frac{\omega b}{U}$ and $C(k)$ is the Theodorsen's function [53]. The aerodynamic lift and moment are obtained by the integration of the difference of pressure along the mean line, i.e.,

$$L(t) = \frac{1}{2}\rho U^2 b\int_0^{\pi} \Delta C_p(\theta, t)\sin\theta \mathrm{d}\theta \tag{8}$$

$$M_0(t) = -\frac{1}{2}\rho U^2 b^2\int_0^{\pi} \left(\cos\theta - \hat{x}_0\right)\Delta C_p(\theta, t)\sin\theta \mathrm{d}\theta \tag{9}$$

where the moment is computed with respect to the point $\bar{x}_0 = x_0/b$. For pitch and plunge harmonic motions, the KS theory leads to results that are equivalent to the classical Theodorsen's theory [52].

The approach used to build a ROM starts from the definition of a parametric model that can be analyzed exploiting the KS theory, followed by a numerical optimization to identify the appropriate values of the parameters through a comparison with CFD experiments.

Exploiting an approach similar to the one used by Liu and Montefort [37], the airfoil is represented by a piecewise-linear mean-line composed by a fixed part plus two movable surfaces: a flap and a tab, see Fig. 12. The first segment represents the airfoil, the second segment models the flap portion of the L-tab, while the last one the effect of the CRV generated by the tab and it extends beyond the TE of the airfoil. This last portion represents a virtual movable surface that can explain the different loads experienced by the airfoil equipped with the L-tab, referred to the

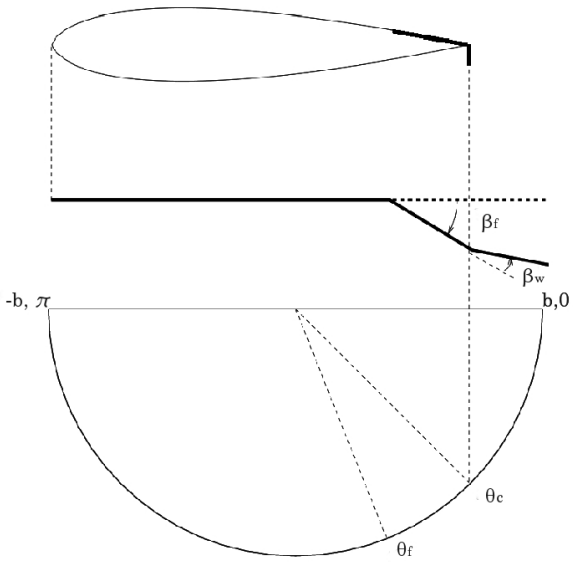

Figure 12. Geometrical parameters of the equivalent KS thin airfoil model.

clean airfoil. In the following, the first segment of the piecewise mean line will be referred to as Equivalent Rigid Airfoil (ERA), the second segment as Equivalent L-Tab (ELT) and the third segment as counter-rotating Vortices Equivalent Trim Tab (VETT).

The geometrical and motion parameters considered for the model order reduction are given in Fig. 12. The parameter x_f indicates the starting point ELT along the chord of the equivalent KS model, and it is expressed through an angle as $\theta_f = \arccos(x_f/b)$. The parameter x_c, and the corresponding angle $\theta_c = \arccos(x_c/b)$, indicates the TE of the airfoil along the chord of the equivalent KS model. The complex parameter $\beta_f \in \mathbb{C}$ represents the amplitude and phase of the ELT rotation relative to the ERA, whereas $\beta_w \in \mathbb{C}$ represents the amplitude and phase of the VETT rotation respect the ELT. All of the geometrical parameters of the KS model are expressed as non-dimensional, using the thin airfoil chord $c_k = 2b$ as the reference quantity. The position θ_c is an extremely important parameter because it represents the fact the KS thin airfoil equivalent model has a longer chord than the physical airfoil, i.e., the point where the Kutta condition must be enforced is not at the airfoil TE. However, to compute the lift and moment to be compared with the CFD simulations, the pressure coefficient in the KS thin airfoil model is integrated from the

leading edge to θ_c, because the last portion of the KS equivalent model is only virtual and does not correspond to a solid structure that can carry loads.

The L-tab equipped airfoil is modeled as a linear system of three degrees of freedom. These are: the pitch of the airfoil, the plunge of the airfoil and the rotation of the L-tab. According to the assumption of linearity of the model, it is possible to study the system response in terms of aerodynamic loads for each of the three aforementioned forcing motions, separately. Furthermore, under the hypotheses of small perturbations and linearity, the upwash velocity can be expressed as:

$$v = v_{\alpha_0}(x) + v_\alpha(x,t) + v_h(x,t) + v_{\beta_0}(x) + v_\beta(x,t) \tag{10}$$

where the subscript α represents the velocity terms from the pitch motion, the subscript h indicates the velocity terms from the plunge motion and the subscript β is related to the velocity terms from the L-tab motion. The velocity contributions related to each of the degrees of freedom can be split into a steady term and a time dependent term, representative of the steady mean value and of unsteady oscillation amplitude, respectively. Accordingly, the aerodynamic forces can be expressed as

$$F = F_{\alpha_0}(x) + F_\alpha(x,t) + F_h(x,t) + F_{\beta_0}(x) + F_\beta(x,t) \tag{11}$$

In the present work pitch oscillations are considered with zero mean value, hence $v_{\alpha_0}(x) = 0$ in Eq. (10). Consistently, it results that $F_{\alpha_0}(x) = 0$ in Eq. (11). A model order reduction procedure is performed separately for each of the remaining terms of Eqs. (10) and (11). The analysis to compute the unsteady loads associated with pitch and plunge motion is not reported here, because it is equivalent to the standard approach presented in Ref. [52, Chapter 13]. For the computation of the lift and moment associated with the ELT and VETT rotations, the equivalent geometry for the ROM takes the following mathematical form

$$z(x,t) = \begin{cases} 0 & \text{if} \quad x \le x_f \\ -(x - x_f)\tilde{\beta}_f e^{j\omega t} & \text{if} \quad x_f < x \le x_c \\ -(x - x_f)\tilde{\beta}_f - (x - x_c)\tilde{\beta}_w e^{j\omega t} & \text{if} \quad x > x_c. \end{cases} \tag{12}$$

The upwash velocity is computed according to Eq. (2) and expressed as a function of θ. It reads

$$v(\theta,t)=\begin{cases}0 & \text{if} \quad \theta>\tilde{\theta}_f \\ -U\left(\mathrm{j}k\cos\theta-\hat{x}_f+1\right)\tilde{\beta}_f\mathrm{e}^{\mathrm{j}\omega t} & \text{if} \quad \theta_f>\theta\geq\theta_c \\ -U\left(\left(\mathrm{j}k\cos\theta-\hat{x}_f+1\right)\tilde{\beta}_f+\left(\mathrm{j}k\cos\theta-\hat{x}_c+1\right)\tilde{\beta}_w\right)\mathrm{e}^{\mathrm{j}\omega t} & \text{if} \quad \theta<\theta_c.\end{cases} \tag{13}$$

The adoption of relative rotations as degrees of freedom allows to build an incremental model for the lift and moment. Consider initially the upwash coefficients and the aerodynamic loads for the ELT, extending from θ_f to θ_c, oscillating with respect to its initial point θ_f, see Fig. 12.

The vertical displacement $z(x,t)$ of the ELT is:

$$z(x,t)=-(x-x_f)\tilde{\beta}_f\mathrm{e}^{\mathrm{j}\omega t}, \qquad x_f<x<x_c \tag{14}$$

where $\tilde{\beta}_f\in\mathbb{C}$ is a complex parameter representing the Fourier transform of the ELT rotation at frequency ω. The vertical perturbation velocity is:

$$v(\theta,t)=-U\left(\mathrm{j}k\left(\cos\theta-\bar{x}_f\right)+1\right)\tilde{\beta}_f\mathrm{e}^{\mathrm{j}\omega t}=g_v(\theta)\mathrm{e}^{\mathrm{j}\omega t}, \qquad \theta_c<\theta<\theta_f \tag{15}$$

with $\bar{x}_f=x_f/b$. The upwash coefficients P_n are then computed through the Fourier transformation of the vertical perturbation velocity, within the interval $[\theta_c \quad \theta_f]$, i.e.,

$$P_n=-\frac{\tilde{\beta}_f}{U\pi}\int_{\theta_c}^{\theta_f}g(\theta)\mathrm{e}^{\mathrm{j}\varphi(\theta)}\cos n\theta\mathrm{d}\theta, \quad \text{where} \tag{16}$$

$$P_0=\frac{\tilde{\beta}_f}{\pi}\left(\mathrm{j}k(\sin\theta_f-\bar{x}_f\theta_f)+\theta_f\right)-\frac{\tilde{\beta}_f}{\pi}\left(\mathrm{j}k(\sin\theta_c-\bar{x}_c\theta_c)+\theta_c\right), \tag{17}$$

$$\begin{aligned}P_1=&\frac{\mathrm{j}k\tilde{\beta}_f}{\pi}\left(\frac{\sin\theta_f}{2}+\frac{\sin 3\theta_f}{6}\right)+\frac{\tilde{\beta}_f}{2\pi}\left(\sin 2\theta_f(1-\mathrm{j}k\bar{x}_f)\right)+\\&-\frac{\mathrm{j}k\tilde{\beta}_f}{\pi}\left(\frac{\sin\theta_c}{2}+\frac{\sin 3\theta_c}{6}\right)-\frac{1}{2\pi}\tilde{\beta}_f\left(\sin 2\theta_c(1-\mathrm{j}k\bar{x}_c)\right),\end{aligned} \tag{18}$$

$$\begin{aligned}P_n=&\frac{\tilde{\beta}_f}{\pi}\left(1-\mathrm{j}k\bar{x}_f\right)\left(\frac{\sin n\theta_f}{n}\right)+\frac{\tilde{\beta}_f}{\pi}\left(\frac{\sin(n+1)\theta_f}{2(n+1)}-\frac{\sin(1-n)\theta_f}{2(n-1)}\right)+\\&-\frac{\tilde{\beta}_f}{\pi}\left(1-\mathrm{j}k\bar{x}_c\right)\left(\frac{\sin n\theta_c}{n}\right)-\frac{\tilde{\beta}_f}{\pi}\left(\frac{\sin(n+1)\theta_c}{2(n+1)}-\frac{\sin(1-n)\theta_c}{2(n-1)}\right)\end{aligned} \tag{19}$$

The series of P_n is convergent toward zero, so it can be truncated after N terms, where N is selected as the first coefficient where the order of magnitude is three times smaller than the leading term of the series.

The A_n coefficients are computed using Eqs. (7). Similarly the computation of ΔC_P through Eq. (5) is straightforward. The aerodynamic loads can be obtained by substituting the resulting expression of ΔC_P in Eqs. (9) and integrating the ΔC_p between the leading edge and the trailing edge at θ_c, i.e.,

$$\begin{aligned} C_\ell &= \frac{1}{2}\int_{\theta_c}^{\pi}\left(4A_0\tan\frac{\theta}{2}+8\sum_{n=1}^{N}A_n\sin n\theta\right)\sin\theta\mathrm{d}\theta \\ &= 2A_0\left(\pi-\theta_c+\sin\theta_c\right)+A_1 2\pi+A_1\frac{\sin 2\theta_c}{4}-A_1 2\theta_c+ \\ &\quad +4\sum_{n=2}^{N}A_n\left(\frac{(n-1)\sin(n+1)\theta_c+(n+1)\sin(1-n)\theta_c}{2n^2-2}\right) \end{aligned} \tag{20}$$

The moment coefficient related to the mid-chord is

$$\begin{aligned} C_m &= -\frac{1}{4}\int_{\theta_c}^{\pi}\left(4A_0\tan\frac{\theta}{2}+8\sum_{n=1}^{N}A_n\sin n\theta\right)\sin\theta\cos\theta\mathrm{d}\theta \\ &= A_0\left(\frac{\pi}{2}-\frac{\sin 2\theta_c}{4}+\sin\theta_c-\frac{\theta_c}{2}\right)+ \\ &\quad +2A_1\frac{\sin^3\theta_c}{3}-A_2\frac{\pi}{2}+A_2\frac{\sin 4\theta_c}{8}-A_2\frac{\theta_c}{2}+ \\ &\quad -2\sum_{n=3}^{N}\left(\frac{(n-2)\sin(n+2)\theta_c-(n+2)\sin(n-2)\theta_c}{4n^2-16}\right) \end{aligned} \tag{21}$$

An identical approach can be used to compute the lift and moment coefficient from the rotation of the VETT.

Numerical computations were carried out on a NACA 0012 section equipped with the L-tab, for pitch and plunge oscillations and tab harmonic motions, at several values of the reduced frequency. The ROM is determined by means of an optimization procedure performed at a fixed reduced frequency. The objective of the optimization is the minimization of the error between the steady mean value or the first harmonic component of CFD-computed lift and moment coefficients and the corresponding quantities computed using the KS model of Fig. 12. The higher harmonic

content from nonlinear effects Ref. [40] is not considered here because the linear KS approach cannot model such effects. In fact, the response at the same frequency of the tab activation is the main concern when harmonic vibration control algorithms, such as the classical Higher Harmonic Control (HHC) [16], are considered in rotorcraft applications. A least squares-based optimization algorithm is used for the minimization procedure. In particular, the function to be minimized is written as follows:

$$f(\mathbf{p}) = \frac{1}{\Re(C_{\ell_{\text{NUM}}})^2}\,\Re(C_{\ell_{\text{NUM}}} - C_{\ell_K}(\mathbf{p}))^2 + \frac{1}{\Im(C_{\ell_{\text{NUM}}})^2}\,\Im(C_{\ell_{\text{NUM}}} - C_{\ell_K}(\mathbf{p}))^2 + \\ + \frac{1}{\Re(C_{m_{\text{NUM}}})^2}\,\Re(C_{m_{\text{NUM}}} - C_{m_K}(\mathbf{p}))^2 + \frac{1}{\Im(C_{m_{\text{NUM}}})^2}\,\Im(C_{m_{\text{NUM}}} - C_{m_K}(\mathbf{p}))^2 \tag{22}$$

where $C_{\ell_{\text{NUM}}}$ and $C_{m_{\text{NUM}}}$ are the first harmonic components of lift and moment coefficients computed from the CFD simulations. The array $\mathbf{p}$ contains the geometrical and motion free parameters of the KS model discussed above, see also Fig. 12, i.e. $\mathbf{p} = \{\theta_c, \theta_f, \tilde{\beta}_f, \tilde{\beta}_w\}$, and it is composed of six independent parameters.

For the steady simulations, the solver output loads are directly used in Eq. (22), which has no imaginary terms. $C_{\ell_K}(\mathbf{p})$ and $C_{m_K}(\mathbf{p})$ are the KS aerodynamic loads to be computed by the optimization algorithm according to the free parameters in $\mathbf{p}$. Depending on the sectional degree of freedom under consideration, different sets of free parameters are selected among all those of the KS formulation. A multistart approach is used to perform the minimization to avoid the identification of a local minimum that does not correspond to the global one. Additionally, to achieve physically consistent solutions, constraints were imposed a priori to the free parameters.

IV. Steady Airfoil with L-tab in Fixed Position

The present section deals with the ROM developed for the airfoil at zero angle of attack with the L-tab in arbitrarily fixed position. According to Eqs. (10) and (11), the transfer function between $v_{\beta_0}(x)$ and $F_{\beta_0}(x)$ must be determined. This analysis will identify the equivalent modification of the airfoil camber and chord extension referred to the position of the L-tab.

A. Steady State Numerical Simulations

Steady state computations were carried out to investigate the influence of the L-tab Gurney flap on the aerodynamic loads and on the flow field.

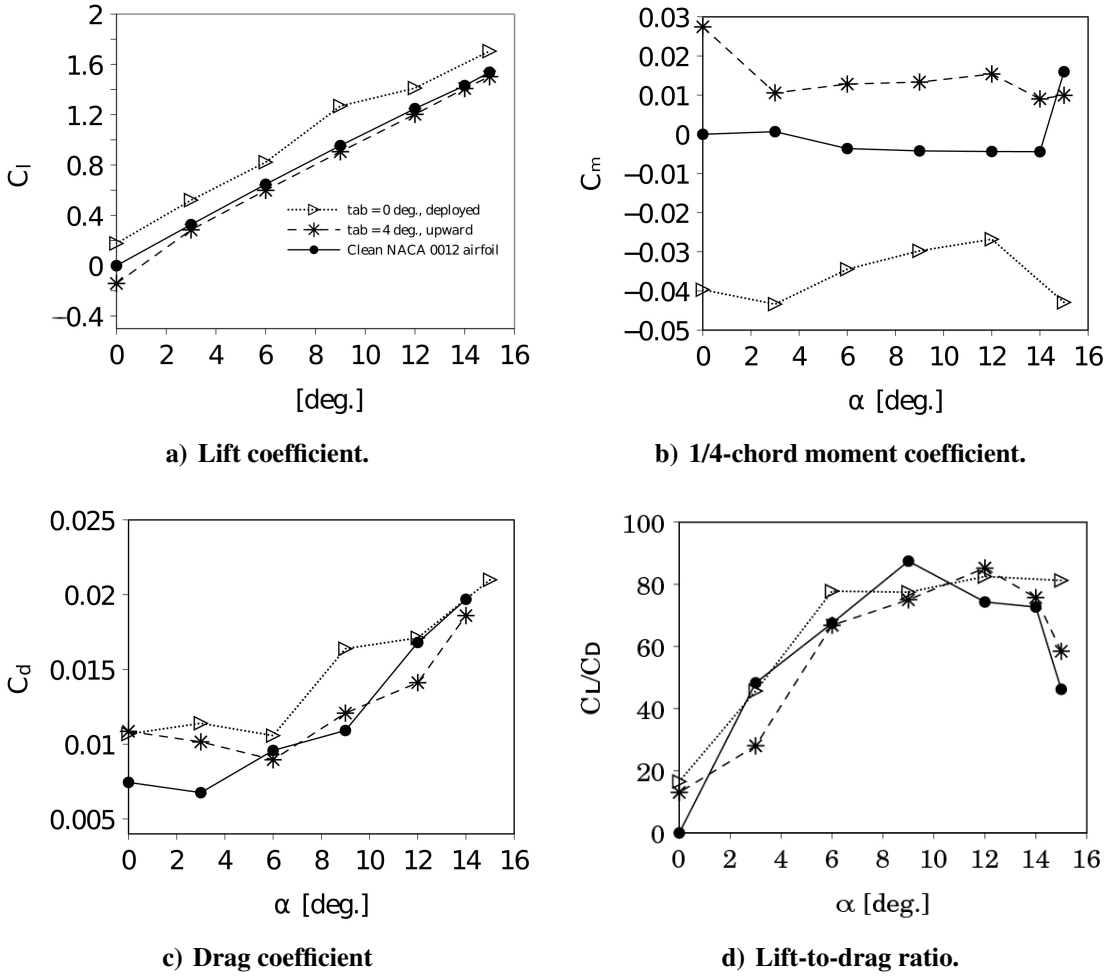

a) Lift coefficient. **b) 1/4-chord moment coefficient.**

c) Drag coefficient **d) Lift-to-drag ratio.**

Figure 13. Steady force coefficients and lift to drag ratio vs. angle of attack for the L-tab downward deflected and in the baseline configuration (four degrees upward deflected). The curves related to the NACA 0012 clean airfoil are also reported.

Figure 13a shows the lift coefficient versus the angle of attack for the baseline configuration, i.e., $\beta_{\text{L-tab}} = 4$ degrees, and for the L-tab downward deflected, i.e., $\beta_{\text{L-tab}} = 0$. The corresponding curve for the clean NACA 0012 geometry is also shown. It can be noticed that in these cases, for attached flow conditions the slope of the C_L-α curve for the L-tab equipped section is almost equal to the slope of the clean airfoil curve, consistently with what has been observed by other authors, see Refs. [5, 8, 13, 25, 32, 54, 55]. When the L-tab is deflected at $\beta_{\text{L-tab}} = 0$, the lift curve shifts

vertically with respect to the clean section, while the baseline angular configuration of the L-tab recovers almost the same lift of the clean airfoil. The primary effect induced by the present device is a change of the airfoil section camber and, as a consequence, a shift in the negative direction of the zero lift angle. When the L-tab is deflected upward, the zero lift angle shifts in the positive direction, with a consequent displacement of the lift curve below the curve of the clean airfoil.

Figure 13b shows the 1/4-chord pitching moment coefficient C_m versus the angle of attack. The behavior of the pitching moment is also affected by the change in the effective camber introduced by the L-tab. The camber modification yields a chordwise shift of the aerodynamic center. In particular, for upward deflections of the movable device, the C_m is lower in magnitude with respect to the clean configuration, at least for small to medium angles of attack. However, when the L-tab is downward deployed, the pitching moment curve lies below the clean airfoil curve.

Figure 13c shows the computed drag coefficient C_d. No penalty in terms of drag was seen with respect to the clean airfoil. These findings are partially supported by the unsteady results of Zanotti [35] where, in the upstroke phase, the measured pressure drag exhibits similar behaviors. For some angles of attack Fig. 13c shows a slight decrease in drag when the L-tab is deflected upward. For upward deflections of the L-tab, the movable device acts similar. Cusher [56] gave an extended review on TE flap-like devices able to reduce the drag compared to the clean configuration, including devices not dissimilar to the present L-tab. Giguère et al. [11] provided a detailed explanation of the physical mechanisms, which, even at low angles of attack, could give a drag reduction, if the GF is properly sized.

Cole at al. [29] showed that for some specific configurations and for angles of attack in the range [5 10] degrees, lower drag coefficients could be attained with a GF. The reverse was found by employing other airfoil-GF configurations, leading Cole at al. to conclude that the performance and effectiveness of a GF is dependent on the shape of the movable device and of the clean airfoil which is used. Consequently, it is possible to infer that the system airfoil plus GF-like actuation system can be designed at least to avoid sharp increase in the drag coefficient.

The lift-to-drag ratio of the airfoil with the L-tab, Fig. 13d, is close to those of the clean airfoil.

B. Reduced Order Model for Steady Airfoil with Fixed L-tab

The numerical results highlight how steady aerodynamic loads undergo significant changes according to deflections of the L-tab. Modifications in the effective aerodynamic shape are twofold. First, as for a classical TE flap, the geometry is modified in camber with respect to the clean configuration. Secondly, the CRV lead to a further variation in camber and increase the effective chord.

To develop a ROM that can reproduce these effects, an extension of the KS model to steady flows can be used, resulting in a model equivalent to the the classical thin airfoil theory. For a steady deflection of the L-tab, a time independent velocity distribution is herein used to compute the upwash coefficients of the KS formulation. As a consequence, $v(x)$ is computed using Eq. (2) with the partial derivative with respect to time set to zero.

According to the approach outlined previously and referring to Eqs. (10) and (11), the transfer function between $v_{\beta_0}(x)$ and $F_{\beta_0}(x)$ can be derived. To consider both the flap-like effects and the Gurney flap-like effects, two free parameters in the KS model are used. These are $\beta_f \in \mathbb{R}$ and $\beta_w \in \mathbb{R}$, which are the deflection angle of the ELT and of the VETT in the piecewise mean line of the KS model. Therefore, the functional is minimized with respect to these two variables. Preliminary investigations showed that the functional is far from regular with several local minima, so additional constraints have been added to the parameters. Such constraints fix the range of the parameters, allowing the achievement of a physically consistent solution. Namely, β_f and β_w were constrained to the range $[-20 \quad 20]$ deg. The remaining geometrical parameters required by the KS formulation are fixed a priori before the optimization procedure, according to the results of the reference numerical model. The chordwise position of the ELT hinge is set to $x_f = 0.6c_k$ so that the ELT covers the 5% of the mean line length, as is the physical size of the ELT.

Numerical results show that the first intersection point of the upper and lower side streamlines is located approximately $20\%c$ past the TE for the present L-tab. As a consequence $\cos\theta_c = 0.8c_k$ is imposed.

Figures 14a and 14b show the values of the ROM parameters obtained through the optimization procedure, as performed at several deflections of the L-tab. The value of β_f is found to increase

with the upward deflection of the L-tab. The presence of a negative β_f for the L-tab deflected downward, reproduces the local increase of camber in TE area by the presence of the GF. A change of behavior is visible at $\beta_{\text{L-tab}}$ around 2 deg., for both parameters. The switch from the first to the second regime occurs when the L-tab does not protrude from the airfoil lower side. When this happens, the stagnation flow region upstream the L-tab disappears, with consequent changes in the overall flow field and in the resulting circulation. Therefore, the pressure distribution, and hence the aerodynamic loads, are modified. Notice that β_w is always negative. In the range $\beta_{\text{L-tab}} = [0 \quad 2]$ degrees, the slope of the β_w-$\beta_{\text{L-tab}}$ curve is positive, whereas the opposite is observed for larger rotations of the tab.

The linear trend of aerodynamic loads and the smoothness of the geometrical parameters versus the L-tab deflection, except for the sharp points at $\beta_{\text{L-tab}} = 2$, suggest that these ROMs may be feasible to compute the equivalent thin geometry and the aerodynamic loads for an arbitrary value of $\beta_{\text{L-tab}}$ in the range of tested angles.

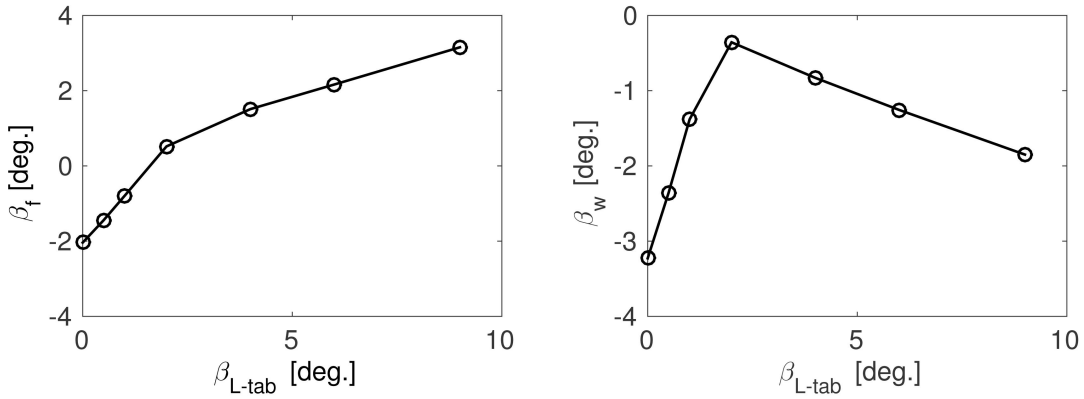

a) Deflection angle of of the ELT. **b) Deflection angle of of the VETT.**

Figure 14. Equivalent deflections of the ELT and of the VETT identified for several angular positions of the L-tab, $\alpha = 0$ deg.

Figures 15a and 15b show the lift and mid-chord moment coefficients computed through the ROM, compared to the corresponding loads predicted by CFD, for several deflections of the L-tab. Good accuracy of the ROM is found, both in terms of C_ℓ and C_m. Again, two almost linear regimes are observed.

Figure 16 shows the equivalent thin line geometry overlapped with the numerical flow field

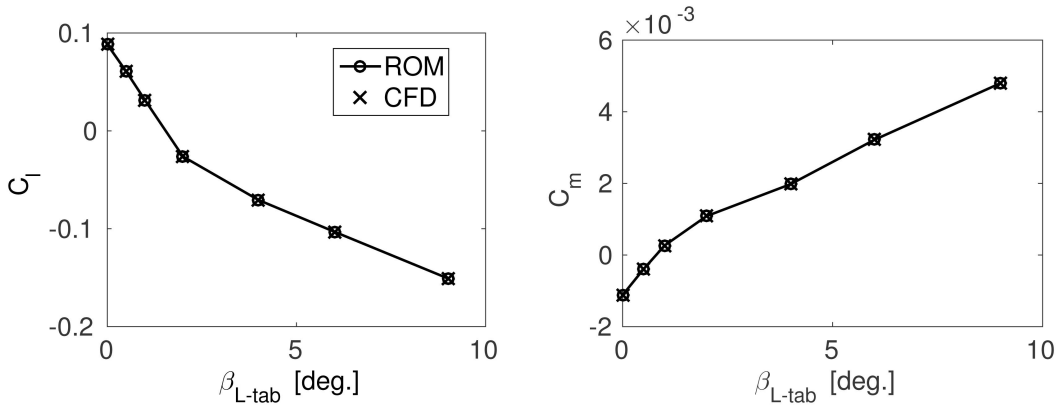

a) Lift coefficient. **b) Mid-chord moment coefficient.**

Figure 15. Lift and mid-chord moment coefficients from the ROM compared to the reference numerical value, for several deflections of the L-tab, $\alpha = 0$ deg.

close to the TE. The dotted line represents the direction parallel to the longitudinal edge of the numerical L-tab, whereas the dashed line is the linear approximation of the zero vorticity line in the CRV region. This latter segment is used to easily locate the mean line of the CRV wake. The two segments just mentioned are useful to capture the mean line modification effects resulting from the numerical computations, with the L-tab. Moreover two streamlines, one from the upper and one from the lower side, are seen to further identify the CRV region. The dash-dotted line represents the ELT, whereas the solid line is related to the VETT. The equivalent geometry captures the flow physics near the airfoil. Indeed the absolute slopes, as well as the relative inclination of the two KS segments, resemble the mean line effects observed in the simulations, even in terms of the CRV. Results, from both numerical computations and the ROM, highlight how the CRV is almost aligned to the L-tab, as expected for steady state computations. Notice that good agreement, between the numerical and the analytical mean line, is found for all of the L-tab rotations that were considered.

The predictive capabilities of the present ROM were tested for $\beta_{\text{L-tab}} = 7$ degrees. The mean line geometry is computed by extracting the values of the ELT and VETT from the curves reported in Figs. 14a and 14b. The aerodynamic loads are extracted from the curves of Figs. 15a and 15b. Numerical computations were carried out and compared to those achieved with the ROM. The ROM is able to predict the aerodynamic loads from an arbitrary L-tab deflection. A 2.24% error is obtained in terms of the lift coefficient, whereas there is a 5% error in the mid-chord moment

coefficient. Moreover, Fig. 17 highlights that the ROM realistically represents the geometry of the mean line and the mean shape of the CRV. These results confirm that the ROM is useful for preliminary design studies of L-tab equipped aerodynamic sections. Indeed, not only the model allows for a straightforward computation of aerodynamic loads, but also the near body-flow field can be reasonably represented.

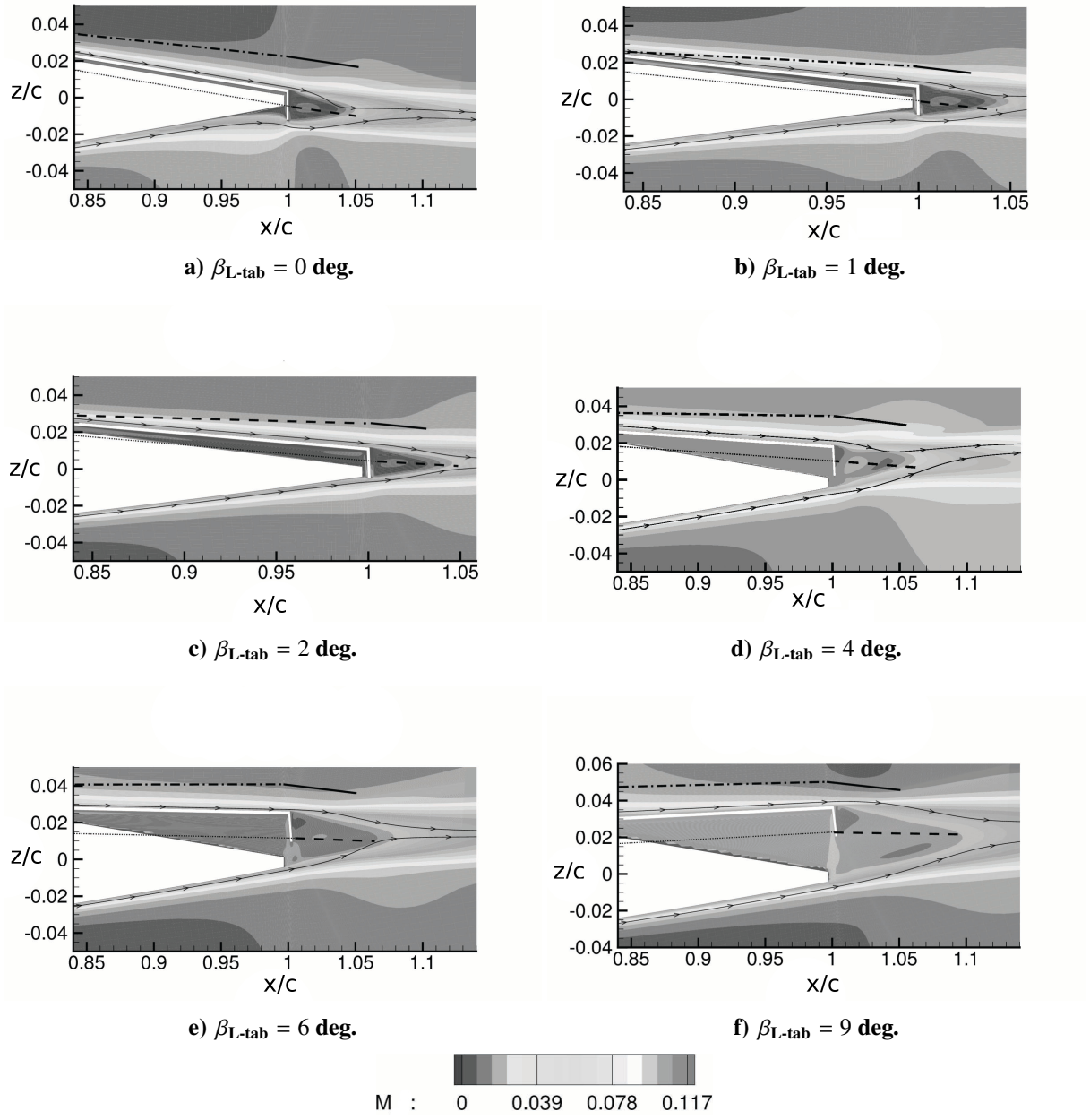

a) $\beta_{\text{L-tab}} = 0$ **deg.** **b)** $\beta_{\text{L-tab}} = 1$ **deg.**

c) $\beta_{\text{L-tab}} = 2$ **deg.** **d)** $\beta_{\text{L-tab}} = 4$ **deg.**

e) $\beta_{\text{L-tab}} = 6$ **deg.** **f)** $\beta_{\text{L-tab}} = 9$ **deg.**

Figure 16. Equivalent geometry for the physical-based thin airfoil ROM, for several deflections of the L-tab overlapped to the numerical Mach number field, together with the streamlines; $\alpha = 0$ degrees; dotted: direction parallel to the longitudinal edge of the numerical L-tab, dashed: linear approximation of the zero vorticity isoline in the wake region, dash-dotted: ELT, solid: VETT.

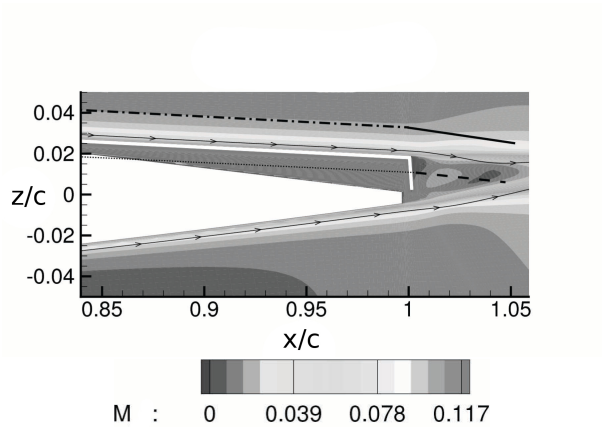

Figure 17. Equivalent geometry for the physical-based thin airfoil ROM, $\alpha = 0$ deg., $\beta_{\text{L-tab}} = 7$ deg.; dotted: direction parallel to the longitudinal edge of the numerical L-tab, dashed: linear approximation of the zero vorticity line in the wake region, dash-dotted: ELT, solid: VETT.

V. Harmonically Pitching and Plunging Airfoil with L-tab in Fixed Position

This section deals with the pitch and plunge motions of the NACA 0012 airfoil, with the L-tab in arbitrary fixed position. These two DOFs are discussed together because of the similarities observed in the hysteresis of the aerodynamic loads. Referring to Eqs. (10) and (11), the transfer functions between $v_\alpha(x,t)$ and $F_\alpha(x,t)$, and between $v_h(x,t)$ and $F_h(x,t)$, are discussed. As in the steady case, the L-tab will affect pressure distribution as well as aerodynamic loads on the whole airfoil. Notice that, for unsteady motions the first harmonic component of aerodynamic loads is extracted from the numerical computations to obtain the linear ROM.

Numerical simulations were carried out for a L-tab equipped NACA 0012 section oscillating in pitch about the 1/4-chord. Computations were also performed for harmonic plunge motions. Oscillations with zero mean value and amplitude of 1 deg. were considered, whereas for the plunge motion the amplitude was set equal to $h/c = 0.01$. Therefore, the equivalent angle of attack $\alpha_{\text{eq}} = \dot{h}/U$ increases linearly with k. However, the change in the equivalent angle of attack does not matter because the behavior of the system is linear.

To check the accuracy of numerical results for pitching/plunging motions, a time convergence analysis was considered for the configuration with the L-tab deployed downward, i.e., $\beta_{\text{L-tab}} = 0$ deg., $k = 0.4$, at $M = 0.117$ and $Re = 10^6$. Figure 18 shows the hysteresis curves of the first harmonic component of the aerodynamic lift and moment due to a pitch oscillation, extracted after 6 and 12 periods, with 200 and 400 time steps per period. There is a good agreement between the lift and moment coefficients. As a consequence, simulation of 6 cycles with 200 time steps per period, were sufficient for numerical simulations of pitching airfoil with the tab in the fixed position. Similar behavior was found for the plunge motion.

However the behavior of the system is slightly nonlinear, because other harmonics are detectable. This behavior has been shown by other authors, see Refs. [32, 40]. Figure 19 points out how lift and moment from pitch and plunge motions may sometime show significant oscillations at frequencies higher than that of the forcing movement.

The first harmonic component of the lift and moment can be estimated with a good precision considering a rigid lifting-line oscillating airfoil. Figures 20 and 21 compare the first harmonic of

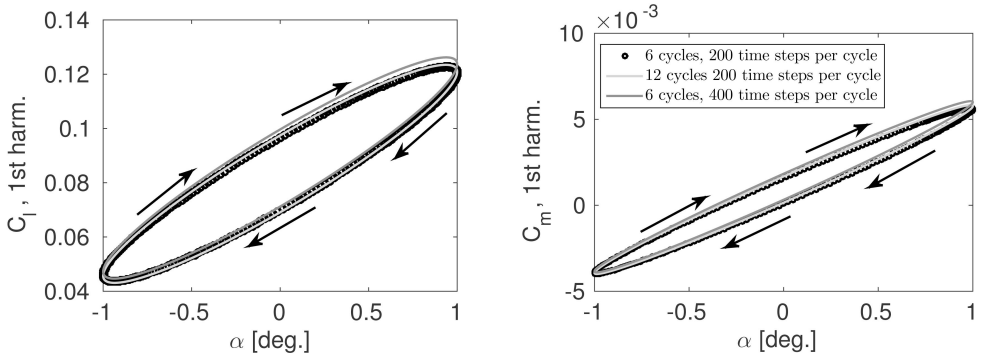

a) Lift coefficient, 1st harmonic.

b) Mid-chord moment coefficient, 1st harmonic.

Figure 18. Time history of force coefficients and first harmonic hysteresis curves for the pitching L-tab equipped NACA 0012 section for twelve oscillation cycles. The convergence is found to be completely achieved after six oscillation cycles, $k = 0.4$**,** $\beta_{\text{L-tab}} = 0$ **deg.**

the airfoil coefficients computed with the CFD with the L-tab in three positions: $\beta_{\text{L-tab}} = 0, 4, 9$ deg. with the curves obtained using the KS based ROM. Errors are found only in the prediction of the moment coefficient in some cases, that might be related to the well known inability of flat-plate models to detect the correct position of the aerodynamic center of thick airfoils [57].

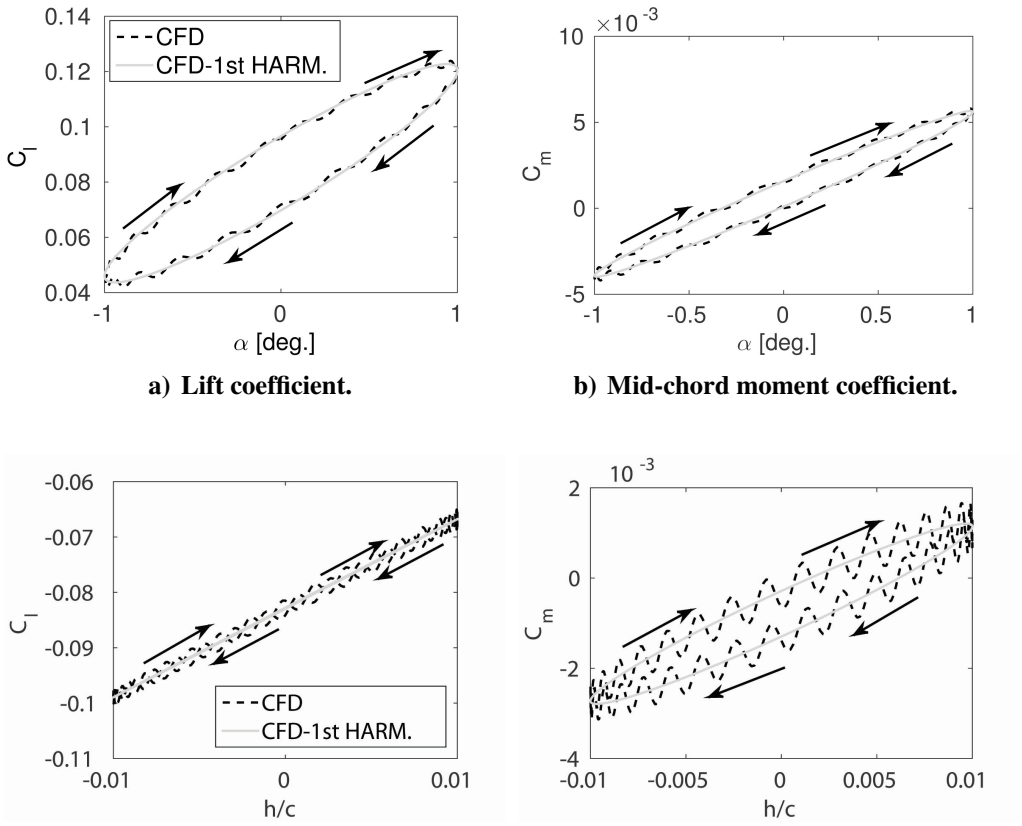

a) Lift coefficient. **b) Mid-chord moment coefficient.**

c) Lift coefficient. **d) Mid-chord moment coefficient.**

Figure 19. Lift and moment coefficients with the corresponding first harmonic component, $\beta_{\text{L-tab}} = 0$ deg., $k = 0.4$. The directions of the hysteresis loops are also reported.

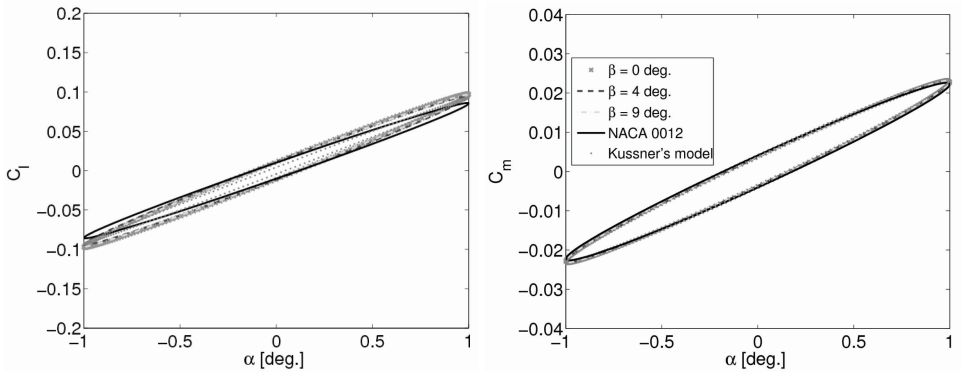

a) C_ℓ**,** $k = 0.1$**, CCW** **b) Mid-chord** C_m**,** $k = 0.1$**, CCW**

c) C_ℓ**,** $k = 0.4$**, CW** **d) Mid-chord** C_m**,** $k = 0.4$**, CW**

Figure 20. First harmonic of lift and moment coefficient from a pitch oscillation for the airfoil with various deflections of the L-tab together with the results for the clean NACA 0012 and the KS ROM results. $\alpha_m = 1$ **deg. The directions of the hysteresis loops are specified: CW clock-wise; CCW counter-clock-wise.**

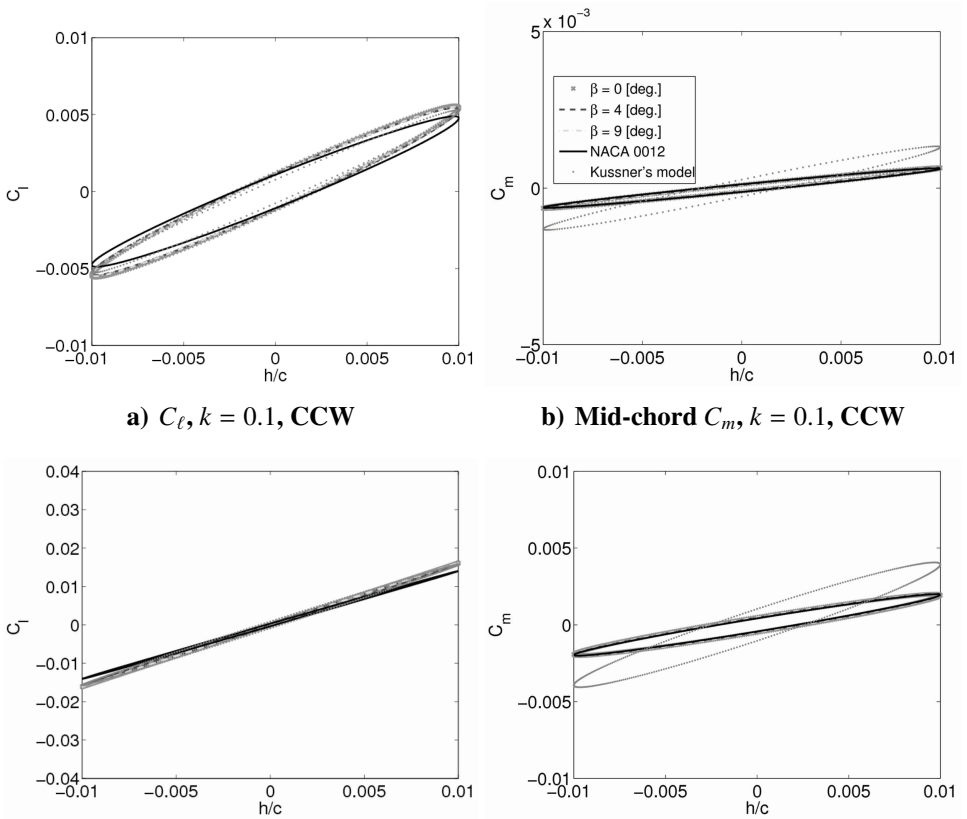

a) C_ℓ**,** $k = 0.1$**, CCW** **b) Mid-chord** C_m**,** $k = 0.1$**, CCW**

c) C_ℓ**,** $k = 0.4$**, CW** **d) Mid-chord** C_m**,** $\mathbf{k} = 0.4$**, CW**

Figure 21. First harmonic of lift and moment coefficient from a plunge oscillation for the airfoil with various deflections of the L-tab together with the results for the clean NACA 0012 and the KS ROM results. $h/c = 0.01$**. The directions of the hysteresis loops are specified: CW clock-wise; CCW counter-clock-wise.**

VI. Steady Airfoil with Harmonically Oscillating L-tab

Finally, the motion of the L-tab was considered. Referring to Eqs. (10) and (11), the transfer function between $v_{\beta(x,t)}$ and $F_{\beta x,t}$ was analyzed. A limited angular rotation of the L-tab, i.e. 1 deg., was considered because a small perturbation ROM model is sought.

A. Reduced Order Model for Airfoil with Harmonically Oscillating L-tab

Because the L-tab is subject to an oscillatory motion, it could be expected that also the CVR will oscillate.

The KS-based ROM was composed of a three segments piecewise lifting line in this case, therefore $\mathbf{p}$ was equal to $\mathbf{p} = [\beta_f,\ \beta_w,\ \theta_c]$, with $\beta_f \in \mathbb{R}$ and $\beta_w \in \mathbb{C}$ to account for the possible phase shift of the CRV motion with respect to the L-tab motion. The length of the ELT is kept fixed at the 20% of the KS model chord, that is $\theta_f = 0.6c_k$, where $c_k = 2b$, while the length of the VETT, and so the θ_c parameter is defined through the optimization. Constraints on the parameters were imposed to drive the minimization algorithm toward a physically consistent solution. Namely, the angle β_f has to be in the range [−9090] deg.; the magnitude of the angle β_f has to be in the range [−1515] deg.; the length of the VETT is constrained to lie in the range 1–10% c.

Figure 22 shows the values obtained of the 4 $\mathbf{p}$ parameters. Overall the chord extension related to the CRV is close to 2.5%c. Figures 22b and 22c show the deflection amplitude of the ELT and of the VETT, respectively. Both these angles grow in magnitude, with opposite sign, for increasing values of k.

Figure 23 compares the first harmonic of the CFD numerical aerodynamic lift and moment to the results obtained with the linear ROM. Good agreement is found in terms of both the lift and moment coefficients for each of the reduced frequencies.

Figure 24 shows the shape of the identified KS-based flat-plate geometry for $k = 0.1$ at four different time instants in the oscillation cycle. To highlight the physical consistency of the present model, the thin-line used by the KS ROM is represented over the geometry and the flow field of the numerical model.

The slope of the ELT is in reasonable agreement with the angular position of the numerical L-

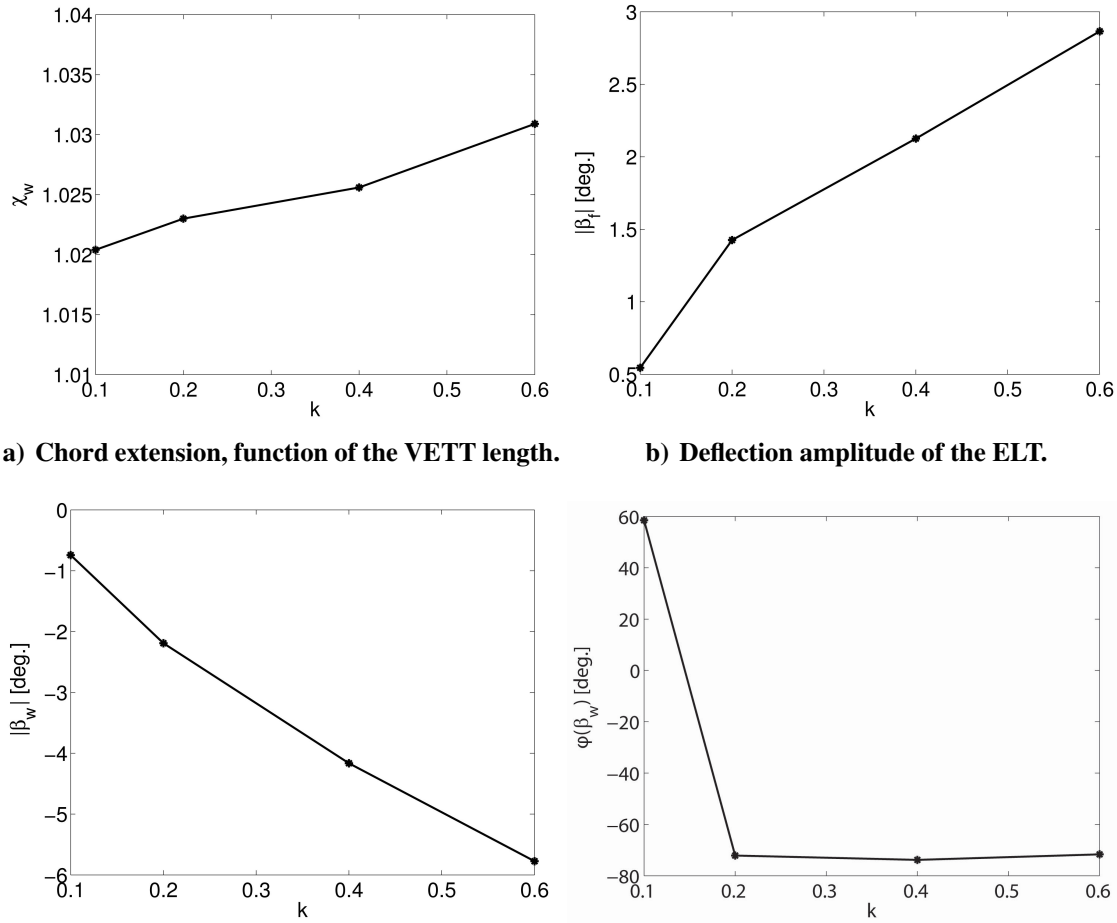

a) Chord extension, function of the VETT length.

b) Deflection amplitude of the ELT.

c) Deflection amplitude of the VETT.

d) Deflection phase of the VETT.

Figure 22. Values of free parameters achieved after the optimization procedure at several reduced frequencies. The first parameter represents the effect of chord extension related to the CRV.

tab, for each of the time steps. A qualitatively good matching with the numerical physics is found in terms length and rotation of the VETT as well. The absolute mean inclination and extension of the CRV are very well captured by the third segment of the piecewise mean line of the ROM. Furthermore, also the relative inclination of the two KS segments shows a good agreement with the numerical mean line effects. The ROM is capable to represent with reasonable accuracy the out-of-phase oscillation of the CRV respect the L-tab, reported in figure 22d. It can be observed that the angle between the L-tab and the CRV, both in numerical computations and in the ROM, is found to be significantly larger than what found for the steady state, discussed previously.

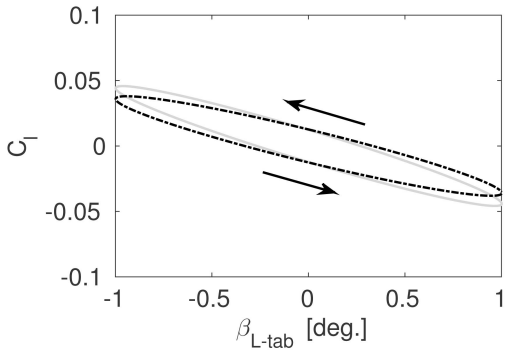

a) Lift coefficient, $k = 0.1$.

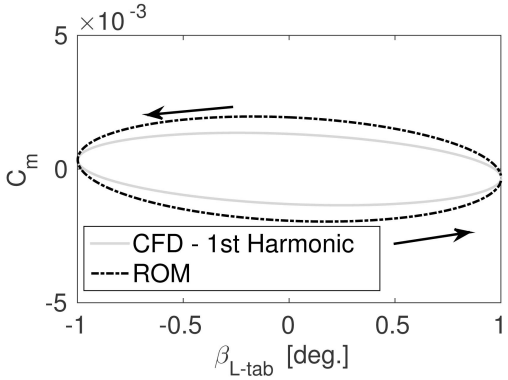

b) Mid-chord moment coefficient, $k = 0.1$.

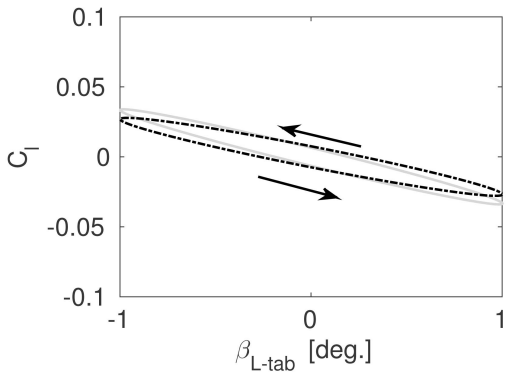

c) Lift coefficient, $k = 0.4$.

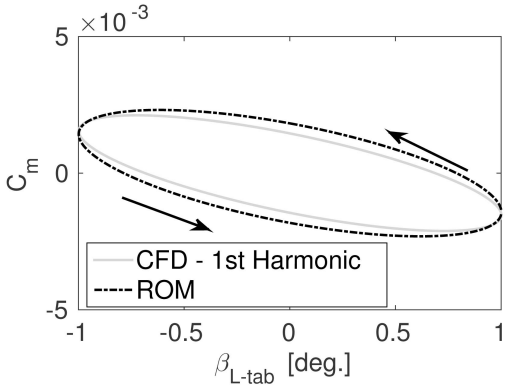

d) Mid-chord moment coefficient, $k = 0.4$.

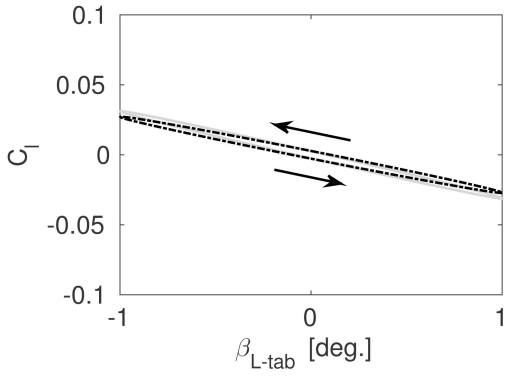

e) Lift coefficient, $k = 0.6$.

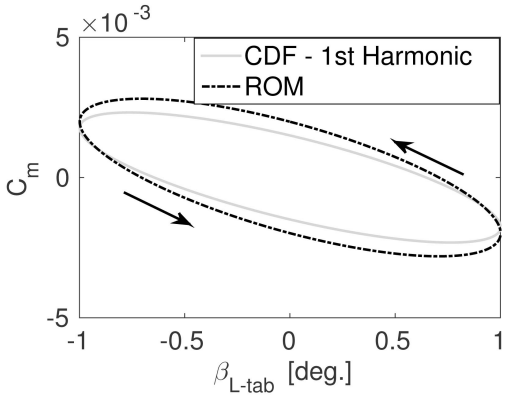

f) Mid-chord moment coefficient, $k = 0.6$.

Figure 23. Comparison of the numerical first harmonic component of aerodynamic loads compared to its counterpart from the KS-based ROM.

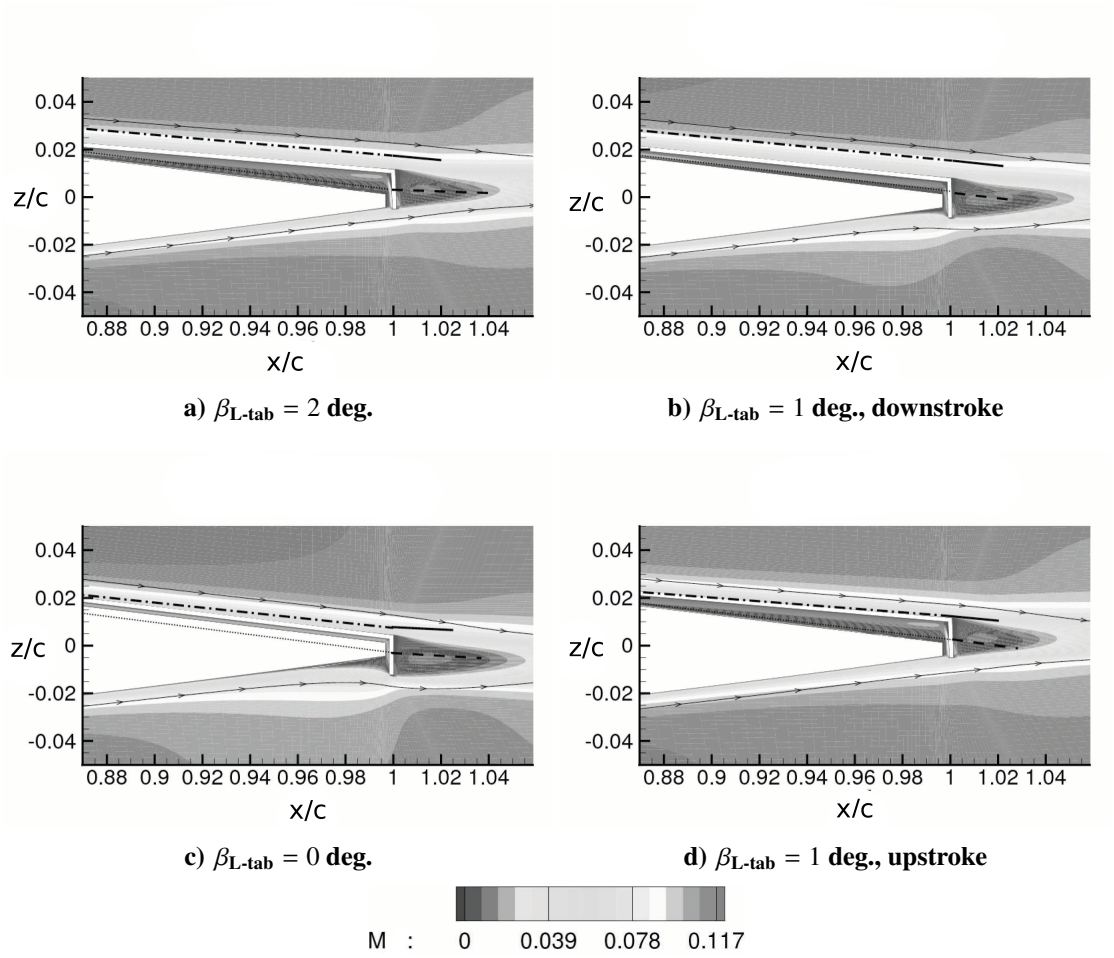

a) $\beta_{\text{L-tab}} = 2$ **deg.**

b) $\beta_{\text{L-tab}} = 1$ **deg., downstroke**

c) $\beta_{\text{L-tab}} = 0$ **deg.**

d) $\beta_{\text{L-tab}} = 1$ **deg., upstroke**

Figure 24. Equivalent geometry for the physical-based thin airfoil ROM, overlapped to the numerical section and to the Mach number field, together with the streamlines; $\alpha = 0$ **deg. Four time steps along the tab oscillation period are represented;** $\beta_{\text{L-tab}} = 1 + 1\sin(\omega t)$ **deg.,** $k = 0.1$**. Dotted: direction parallel to the longitudinal edge of the numerical L-tab; dashed: linear approximation of the zero vorticity level line in the wake region; dash-dotted: ELT; solid: VETT.**

VII. Conclusions

A L-shaped Gurney flap installed on a NACA 0012 section was aerodynamically characterized using numerical simulations. The aerodynamic section with the movable device was treated as a system with three DOFs, i.e., harmonic pitch and plunge motions of the airfoil and the harmonic oscillation of the L-tab. Both steady and unsteady computations were performed to assess the aerodynamic response of the system under constant and time-varying boundary conditions.

The simulations highlighted how the L-tab acts as a Gurney flap when deployed downward, and as a classical TE flap when deflected upward. It was found that the L-tab primarily acts by modifying the effective camber and length of the section. Exploiting the CFD computations a physically consistent ROM, based on the analytical KS linear flat-plate theory was developed. The KS-based ROM was found to appropriately reproduce the changes in shape of the mean line. For unsteady motions, the ROM was capable of reproducing the first harmonic of the aerodynamic loads. The ROM presented essentially extends the bounded vortex area associated to the airfoil to the trailing edge region of the counter rotating vortices generated by the Gurney flap.

Good agreement was found between the loads computed with the KS-based ROM and the numerical results. Specifically, in the steady state the differences in the aerodynamic loads between the CFD and the model were below 0.1%. For oscillating motions of the L-tab, the error between the loads computed with the numerical simulations and with the ROM was 5–8%. Such values are meant in terms of both magnitude and phase of lift and moment coefficient. Furthermore, for the steady case and for the fixed airfoil with the oscillating tab, the equivalent mean line of the ROM was found to accurately reproduce the reference mean line of the numerical geometry. The length and the inclination of the CRV behind the L-tab were also captured by the ROM.

The physical consistency of this ROM may have several advantages compared to black box identification procedures, e.g. rational functions approximations. Indeed it allows to estimate the loads generated by a GF-like movable surface, by simply estimating the size of the CRV area and the phase lag of its oscillation respect the GF. Additionally, this approach is capable to reproduce realistically the near body physics. The availability of these complete information can be very important for the conceptual and preliminary design of a rotorcraft blades active control system.

References

[1] Katz, J., "Aerodynamics of Race Cars," *Annual Review of Fluid Mechanics*, Vol. 38, No. 1, 2006, pp. 27–63,
doi:10.1146/annurev.fluid.38.050304.092016.

[2] Liebeck, R. H., "Design of Subsonic Airfoils for High Lift," *Journal of Aircraft*, Vol. 15, No. 9, 1978, pp. 547–561,
doi:10.2514/3.58406.

[3] Kentfield, J., "The potential of Gurney flaps for improving the aerodynamic performance of helicopter rotors," in "AIAA International Powered Lift Conference," AIAA, 1993, pp. 283–292,
doi:10.2514/6.1993-4883.

[4] Storms, B. L. and Jang, C. S., "Lift Enhancement of an Airfoil Using a Gurney Flap and Vortex Generators," *Journal of Aircraft*, Vol. 31, No. 3, 1994, pp. 542–547,
doi:10.2514/3.46528.

[5] Myose, R. Y., Papadakis, M., and Heron, I., "Gurney Flap Experiments on Airfoils, Wings, and Reflection Plane Model," *Journal of Aircraft*, Vol. 35, No. 2, 1998, pp. 206–211,
doi:10.2514/2.2309.

[6] Papadakis, M., Myose, R. Y., Heron, I., and Johnson, B. L., "An experimental investigation of Gurney flaps on a GA(W)-2 airfoil with 25% slotted flap," in "14th AIAA Applied Aerodynamic Conference, AIAA Paper 1996-2437," , 1996,
doi:10.2514/6.1996-2437.

[7] Zhang, W., Wang, J. J., and Wu, Z., "Experimental investigations on the application of lift enhancement devices to forward-swept aircraft model," *The Aeronautical Journal*, Vol. 110, No. 1108, 2006, pp. 361–367.

[8] Wang, J. J., Li, Y. C., and Choi, K. S., "Gurney flap-Lift enhancement, mechanisms and applications," *Progress in Aerospace Sciences*, Vol. 44, No. 1, 2008, pp. 22–47,
doi:10.1016/j.paerosci.2007.10.001.

[9] Baker, J. P., Standish, K. J., and van Dam, C. P., "Two-Dimensional Wind Tunnel and Computational Investigation of a Microtab Modified Airfoil," *Journal of Aircraft*, Vol. 44, No. 2, 2007, pp. 563–572,
doi:10.2514/1.24502.

[10] Maughmer, M. and Bramesfeld, G., "Experimental Investigation of Gurney flaps," *Journal of Aircraft*, Vol. 45, No. 6, 2008, pp. 2062–2067,
doi:10.2514/1.37050.

[11] Giguère, P., Lemay, J., and Dumas, G., "Gurney Flap Effects and Scaling for Low-Speed Airfoils," in "AIAA 13th Applied Aerodynamics Conference, AIAA Paper 1995-1881," , 1995, pp. 966–976,
doi:10.2514/6.1995-1881.

[12] Jang, C. S., Ross, J. C., and Cummings, R. M., "Numerical Investigation of an Airfoil with a Gurney Flap," *Aircraft Design*, Vol. 1, No. 2, 1998, pp. 75–88,
doi:10.1016/S1369-8869(98)00010-X.

[13] Jeffrey, D., Zhang, X., and Hurst, D., "Aerodynamics of Gurney Flaps on a Single-Element High-Lift Wing," *Journal of Aircraft*, Vol. 37, No. 2, 2000, pp. 295–301,
doi:10.2514/2.2593.

[14] Standish, K. J. and van Dam, C. P., "Computational Analysis of a Microtab-Based Aerodynamic Load Control System for Rotor Blades," in "AHS 4th Decennial Specialist's Conference on Aeromechanics," San Francisco, CA, 2004.

[15] Motta, V., Guardone, A., and Quaranta, G., "Numerical investigation of an L-shaped deployable Gurney tab for rotorcraft vibration control," in "International Forum on Aeroelasticity and Structural Dynamics (IFASD 2013)," Royal Aeronautical Society, Bristol, UK, 2013.

[16] Friedmann, P. P. and Millott, T. A., "Vibration reduction in rotorcraft using active control–A comparison of various approaches," *Journal of Guidance, Control, and Dynamics*, Vol. 18, No. 4, 1995, pp. 664–673,
doi:10.2514/3.21445.

[17] Milgram, J., Chopra, I., and Straub, F., "Rotors with trailing edge flaps: Analysis and comparison with experimental data," *Journal of the American Helicopter Society*, Vol. 43, No. 4, 1998, pp. 319–332,
doi:10.4050/JAHS.43.319.

[18] Roget, B. and Chopra, I., "Robust individual blade control algorithm for a dissimilar rotor," *Journal of guidance, control, and dynamics*, Vol. 25, No. 5, 2002, pp. 915–923,
doi:10.2514/2.4964.

[19] Shen, J., Yang, M., and Chopra, I., "Swashplateless Helicopter Rotor System with Trailing-Edge Flaps for Flight and Vibration Controls," *Journal of aircraft*, Vol. 43, No. 2, 2006, pp. 346–352,
doi:10.2514/1.14634.

[20] Roget, B. and Chopra, I., "Wind-Tunnel Testing of Rotor with Individually Controlled Trailing-Edge Flaps for Vibration Reduction," *Journal of Aircraft*, Vol. 45, No. 3, 2008, pp. 868–879,
doi:10.2514/1.28455.

[21] Greenblatt, D., Nishri, B., Darabi, A., and Wygnanski, I., "Dynamic stall control by periodic excitation, Part 2: mechanisms," *Journal of Aircraft*, Vol. 38, No. 3, 2001, pp. 439–447,
doi:10.2514/2.2811.

[22] Feszty, D., Gillies, E. A., and Vezza, M., "Alleviation of Airfoil Dynamic Stall Moments via Trailing-Edge-Flap Flow Control," *AIAA Jornal*, Vol. 42, No. 1, 2004, pp. 17–25,
doi:10.2514/1.853.

[23] Lee, T. and Lee, L., "Effect of Gurney flap on unsteady wake vortex," *Journal of aircraft*, Vol. 44, No. 4, 2007, pp. 1398–1402,
doi:10.2514/1.29555.

[24] Lee, T. and Gerontakos, P., "Oscillating wing loadings with trailing-edge strips," *Journal of Aircraft*, Vol. 43, No. 2, 2006, pp. 428–436,
doi:10.2514/1.15616.

[25] Tang, D. and Dowell, E. H., "Aerodynamic Flow Control of an Airfoil with Small Trailing-Edge Strips," *Journal of Aircraft*, Vol. 43, No. 6,
doi:10.2514/1.18969.

[26] Tang, D. and Dowell, E. H., "Aerodynamic Loading for an Airfoil with an Oscillating Gurney Flap," *Journal of Aircraft*, Vol. 44, No. 4, 2007, pp. 428–436,
doi:10.2514/1.26440.

[27] Kinzel, M. P., Maughmer, M. D., and Duque, E. P. N., "Numerical investigation on the aerodynamics of oscillating airfoils with deployable Gurney flaps," *AIAA journal*, Vol. 48, No. 7, 2010, pp. 1457–1469,
doi:10.2514/1.J050070.

[28] Li, Y., Wang, J., and Zhang, P., "Influences of Mounting Angles and Locations on the Effects of Gurney Flaps," *Journal of Aircraft*, Vol. 40, No. 3, 2003, pp. 494–498,
doi:10.2514/2.3144.

[29] Cole, J. A., Vieira, B. A., Coder, J. G., Premi, A., and Maughmer, M. D., "Experimental Investigation into the Effect of Gurney Flaps on Various Airfoils," *Journal of Aircraft*, Vol. 50, No. 4, 2013, pp. 1287–1294,
doi:10.2514/1.C032203.

[30] Matalanis, C. G., Wake, B. E., Opoku, D., Min, B.-Y., Yeshala, N., and Sankar, L., "Aerodynamic Evaluation of Miniature Trailing-Edge Effectors for Active Rotor Control," *Journal of Aircraft*, Vol. 48, No. 3, 2011, pp. 995–1004,
doi:10.2514/1.C031191.

[31] Min, B., Sankar, L., and Bauchau, O., "A CFD-CSD Coupled-Analysis of HART-II Rotor Vibration Reduction using Gurney Flaps," in "Proceedings of the American Helicopter Society 66th Forum and Technology Display, Phoenix, Arizona," , 2010.

[32] Liu, L., Padthe, A. K., and Friedmann, P. P., "Computational Study of Microflaps with Application to Vibration Reduction in Helicopter Rotors," *AIAA Jornal*, Vol. 49, No. 7,
doi:10.2514/1.J050829.

[33] Palacios, J., Kinzel, M., Overmeyer, A., and Szefi, J., "Active Gurney Flaps: Their Application in a Rotor Blade Centrifugal Field," *Journal of Aircraft*, Vol. 51, No. 2, 2014, pp. 473–489,
doi:10.2514/1.C032082.

[34] Zanotti, A., Grassi, D., and Gibertini, G., "Experimental Evaluation of an L-Shaped tab to be used as an Active Gurney Flap for Dynamic Stall Control," in "39th European Rotorcraft Forum," Moscow, Russia, 2013, pp. 1–9.

[35] Zanotti, A., Grassi, D., and Gibertini, G., "Experimental investigation of a trailing edge L-shaped tab on a pitching airfoil in deep dynamic stall conditions," *Proceedings of the Institution of Mechanical Engineers, Part G: Journal of Aerospace Engineering*, Vol. 228, No. 12, 2013, pp. 2371–2382,
doi:110.1177/0954410013517089.

[36] Lee, T. and Su, Y., "Lift enhancement and flow structure of airfoil with joint trailing-edge flap and Gurney flap," *Experiments in fluids*, Vol. 50, No. 6, 2011, pp. 1671–1684,
doi:10.1007/s00348-010-1024-8.

[37] Liu, T. and Montefort, J., "Thin-Airfoil Theoretical Interpretation for Gurney Flap Lift Enhancement," *Journal of Aircraft*, Vol. 44, No. 2,
doi:10.2514/1.27680.

[38] Kinzel, M. P., Maughmer, M. D., and Lesieutre, G. A., "Miniature Trailing-Edge Effectors for Rotorcraft Performance Enhancement," *Journal of the American Helicopter Society*, Vol. 52, No. 2, 2007, pp. 146–158,
doi:10.4050/JAHS.52.146.

[39] Hariharan, N. and Leishman, J. G., "Unsteady Aerodynamics of a Flapped Airfoil in Subsonic Flow by Indicial Concepts," *Journal of Aircraft*, Vol. 33, No. 5, 1996, pp. 855–868, doi:10.2514/3.47028.

[40] Vieira, B., Kinzel, M., and Maughmer, M., "Unsteady Aerodynamics of Miniature Trailing-Edge Effectors Based on Indicial Methods," in "49th AIAA Aerospace Sciences Meeting, AIAA Paper 2011-1049," , 2011, doi:10.2514/6.2011-1049.

[41] Küssner, H. and Schwarz, L., "The oscillating wing with aerodynamically balanced elevator," TM 991, NACA, 1941. Translated from Luftfahrtforschung, vol. 17, pp. 337–354, 1940.

[42] Richter, K. and Rosemann, H., "Experimental investigation of trailing-edge devices at transonic speeds," *Aeronautical Journal*, Vol. 106, No. 1058, 2002, pp. 185–193.

[43] Li, Y., Wang, J., and Hua, J., "Experimental investigations on the effects of divergent trailing edge and Gurney flaps on a supercritical airfoil," *Aerospace Science and Technology*, Vol. 11, No. 2, 2007, pp. 91–99, doi:10.1016/j.ast.2006.01.006.

[44] Biava, M., *RANS computations of rotor/fuselage unsteady interactional aerodynamics*, Ph.D. thesis, Politecnico di Milano, 2007.

[45] Spalart, P. R. and Allmaras, S. R., "A One Equation Model For Aerodynamic Flows," in " 30th Aerospace Sciences Meeting and Exhibit," , 1992. AIAA Paper 1992-0439.

[46] van Leer, B., "Towards the ultimate conservative difference scheme. IV. A new approach to numerical convection," *Journal of Computational Physics*, Vol. 23, No. 3, 1977, pp. 276–299.

[47] van Leer, B., "Towards the ultimate conservative difference scheme. V. A second-order sequel to Godunov's method," *Journal of Computational Physics*, Vol. 32, No. 1, 1979, pp. 101–136.

[48] Venkatakrishnan, V. and Mavriplis, D., "Implicit method for the computation of unsteady flows on unstructured grids," *Journal of Computational Physics*, Vol. 127, No. 2, 1996, pp. 380–397.

[49] Antoniadis, A., Drikakis, D., Zhong, B., Barakos, G., Steijl, R., Biava, M., Vigevano, L., Brocklehurst, A., Boelens, O., Dietz, M., et al., "Assessment of CFD methods against experimental flow measurements for helicopter flows," *Aerospace Science and Technology*, Vol. 19, No. 1, 2012, pp. 86–100, doi:10.1016/j.ast.2011.09.003.

[50] Biava, M., Khier, W., and Vigevano, L., "CFD prediction of air flow past a full helicopter configuration," *Aerospace Science and Technology*, Vol. 19, No. 1, 2012, pp. 3–18, doi:10.1016/j.ast.2011.08.007.

[51] Abbott, I. and von Doenhoff, A., *Theory of Wing sections*, Dover Publication, Inc., New York, NY, 1949.

[52] Fung, Y., *Theory of Aeroelasticity*, John Wiley and Sons, Inc., New York, 1955.

[53] Theodorsen, T., "General Theory of Aerodynamic Instability and the Mechanism of Flutter," TR 496, NACA, 1935.

[54] Traub, L. W. and Agarwal, G., "Exploratory investigation of geometry effects on Gurney flap performance," *Journal of aircraft*, Vol. 44, No. 1, 2007, pp. 349–351, doi:10.2514/1.28385.

[55] Yu, T., Wang, J., and Zhang, P., "Numerical simulation of Gurney flap on RAE-2822 supercritical airfoil," *Journal of Aircraft*, Vol. 48, No. 5, 2011, pp. 1565–1575, doi:10.2514/1.C031285.

[56] Cusher, A. A., *A Design and Analysis Approach for Drag Reduction on Aircraft with Adaptive Lifting Surfaces* , Ph.D. thesis, 2008.

[57] Leishman, J. G., *Principles of Helicopter Aerodynamics*, Cambridge University Press, 2006.